Fabrication and Characterization of Novel Zinc Air Battery Cathodes Using Electrospinning and Electrospraying Techniques

by

Ellsworth Bell

A thesis

presented to the University Of Waterloo

in fulfilment of the

thesis requirement for the degree of

Master of Applied Science

in

Chemical Engineering

Waterloo, Ontario, Canada, 2021

Author's Declaration

I hereby declare that I am the sole author of this thesis. This is a true copy of the thesis, including any required final revisions, as accepted by my examiners.

I understand that my thesis may be made electronically available to the public.

Statement of Contributions

Many of the instruments used in this work were conceived, built, and designed by other members of the PMEAL research group. The electrospinning apparatus was originally built by Matt Kok. Yongwook Kim built the electrospraying apparatus and effective diffusivity instrument. The device used to evaluate breakthrough pressure was built by Jeff Gostick. Other members of the PMEAL group have modified and improved upon the original designs as needed. The work contained in this thesis would not have been possible without these efforts.

Abstract

High specific energy density, low cost, and relative safety make zinc air batteries a promising energy storage technology. However, to fully realize their advantages improvements must be made to increase their efficiency, in terms of both energy and power density. This work focuses on designing novel cathode materials for zinc air flow batteries with improved mass transport and electrochemical properties. Electrospinning and electrospraying techniques were used to develop highly porous gas diffusion layers and high surface area catalyst layers, respectively. The physical characteristics of these materials were evaluated and compared to a commercial cathode material. Electrospun fiber mats were shown to offer favorable mass transport characteristics over the reference material, and electrosprayed catalyst layers offered high specific surface area. A test cell was designed and used to evaluate the electrochemical performance of the cathode materials in this work. Results of those experiments showed that electrosprayed catalyst layers performed better than the reference material, and that more development of electrospun and electrosprayed materials is justified.

Acknowledgements

I'd like to thank Jeff Gostick for the opportunity to join his research group and for all the time he committed, especially the many scheduled and unscheduled meetings that made this work possible. Without his calm and patient guidance completing this project while navigating campus closures and equipment failures would have been a much different experience.

I've enjoyed working with and getting to know the entire PMEAL group and would especially like to thank Awais for his instruction on producing electrospun materials and Yong for his sharing his expertise in a variety of instruments as well as his supernatural ability to locate almost anything in the lab. Yong also helped me by taking some SEM images when I was a little overwhelmed with other experiments.

And, of course, I'm grateful for the support of my friends and family over the past two years, and for their patience. I couldn't have done it without them.

Table of Contents

List of Figures

List of Tables

1 Introduction

Prior to COVID-19, electricity demand had been increasing annually for decades, and although the pandemic has reduced total electricity demand, demand for renewable energy specifically increased by 1.5% in Q1 of 2020. This is largely due to new solar projects coming online and the fact that renewable electricity producers are not required to modulate production to meet demand in way that conventional electricity producers are [1]. Renewable electricity generation is a means to reduce greenhouse gas emission by reducing the need for conventional thermal electricity production. Unlike conventional electricity generation, many sources of renewable energy are intermittent, with peak production not aligning with peak demand. In the extreme cases, renewable energy production could outpace consumer demand during peak production, causing inefficient energy utilization and even destabilize the grid. Simulations have shown that when renewable electricity production accounts for 25-30% of annual demand energy storage becomes necessary to ensure electrical grid stability [2].

Many different forms of renewable energy storage currently exist, serving different purposes. Electrochemical energy storage solutions offer a high degree of flexibility, allowing different power and energy requirements to be met. When integrated with electricity generated from photovoltaic cells and wind turbines, batteries reduce the temporal fluctuations in energy production, absorbing excess power generation and hence acting as a buffer. Batteries thus increase grid stability and reduce energy cost by serving as load shifting solutions, storing energy produced at a time of low demand and making it available when demand, and price, increases

[3].

Zinc – air batteries (ZAB) are a particularly promising electrochemical technology as they offer a relatively high energy density, enabling them to store large amounts of electricity produced at off peak hours. However, the technology is still being developed, and more research is needed to reduce cost, improve performance, and extend operating life. The work contained in this thesis is motivated by a desire to improve zinc-air battery performance by improving mass transport and catalyst layer morphology at the air cathode.

1.1 Zinc – air batteries

1.1.1 Overview

The high energy density and the fact that oxygen from the air is one of the reactants make metal - air batteries an attractive electrochemical energy storage solution. Zinc and lithium have garnered the most attention as anode metals, with zinc offering safety advantages over highly reactive lithium in addition to being plentiful and fully recyclable. Large scale lithium ion energy storage costs approximately $150 per kWh, while zinc air battery storage currently costs ~$100 per kWh, largely due to the lower cost of zinc [4]. Primary zinc air batteries, which are not electrically rechargeable have been commercially viable for years. Button cells commonly used to power hearing aids are an example. In secondary zinc air batteries, the anode metal consumed during discharge is regenerated by recharging the cell. Both primary and secondary batteries are being developed for renewable energy storage.

Primary batteries are recharged by supplying fresh zinc, refined by

electrowinning using power from excess renewable energy, to the cell. These primary batteries can be conceptualized as “mechanically rechargeable” cells, where the anodic material is continually supplied to the cell. In this sense they are effectively fuel cells, with the anodic fuel, zinc metal in this instance, and cathodic fuel, oxygen, being continually delivered to the cell.

Table 1 A comparison of electrochemical properties for zinc and lithium air cells[5]

Anode Metal	Electrochemical equivalent of metal (Ah/g)	Theoretical specific energy of metal (kWh/kg)	Valence charge	Theoretical cell voltage*	Practical cell voltage
Zn	0.82	1.3	2	1.6	1.0 – 1.2
Li	3.86	13.0	1	2.9	2.4

*with an oxygen cathode

Large scale zinc - air batteries have four primary components, the anode, cathode, electrolyte, and separator. The anode is zinc metal, usually in powder form. During discharge zinc is oxidized, liberating two electrons for every atom. Various anode structures have been explored with the goal of improving efficiency by increasing surface area[6], [7]. Potassium hydroxide (KOH) at high concentrations (~6M), is the traditional electrolyte used in zinc – air batteries, providing a high ionic conductivity and preventing the formation of insoluble zinc species in the cell[8]. A separator keeps the cathode and anode electrically isolated, preventing short circuits, while also allowing hydroxide ions to diffuse to and from the air cathode during operation. Oxygen is reduced at the cathode during discharge. The cathode must be porous to allow oxygen to reach the catalyst layer where reduction occurs, while also not allowing electrolyte to invade the pore structure and flooding the cell. The overall reaction occurring in ZABs is given in chemical Eq. 1:

$$2Zn + O_2 + 2H_2O \rightarrow 2Zn(OH)_2 \qquad \textbf{Eq. 1}$$

In the following sections the electrochemistry and engineering challenges of the anode and cathode are discussed in more detail.

1.1.2 Anode

This thesis focuses on the cathode of a zinc air battery, but an understanding of the anode side is important. The anode, pure zinc metal powder, can be conceptualized as the part of a zinc – air cell where energy is stored. Each zinc atom contains two valence electrons that are liberated during discharge. Zinc structures with high porosity are used as anode materials. Increasing the number of active sites on the surface enables discharge at higher rates while minimizing voltage losses[9]. Zinc powder with porosity values of 60-80% has a specific energy capacity of 1.2 – 2.2 Ah/cm^2[10].

A concentrated KOH solution is the most commonly used electrolyte in zinc – air batteries due to its high ionic conductivity. During discharge the zinc anode undergoes various chemical processes, including solvation into ions and oxidation of surface atoms in the solid zinc [10]. Both solubility and the ionic species formed during dissolution is a function of pH. For example, ZnO and $Zn(OH)_2$ are insoluble compounds that form in solutions of ~8-13 pH. Alkaline electrolyte solutions with a pH of ~14 are used to avoid formation of insoluble compounds.

The reaction scheme for the oxidation of zinc in an alkaline solution is as follows:

$$Zn \rightarrow Zn^{2+} + 2e^{-} \quad \textbf{Eq. 2}$$

$$Zn^{2+} + 4OH^{-} \rightarrow Zn(OH)_4^{2-} \quad \textbf{Eq. 3}$$

$$Zn(OH)_4^{2-} \rightarrow ZnO + H_2O + 2OH^{-} \quad \textbf{Eq. 4}$$

$$Zn + 2H_2O \rightarrow Zn(OH)_2 + H_2 \quad \textbf{Eq. 5}$$

During discharge zinc is oxidized, Eq. 3, first forming zincate ($Zn(OH)_4^{2-}$), then zinc oxide (ZnO), shown in Eq. 4. ZnO formation is not reversible. Secondary batteries must be engineered to avoid ZnO formation, while primary cells can be recharged by removing ZnO from the anode compartment and replenishing the cell with zinc metal.

When charging a secondary zinc – air cell, hydrogen evolution at the anode is possible, this reaction is given by chemical Eq. 5, and is actually two simultaneous reactions, Eq. 2 and Eq. 6,that occur at the anode and cathode respectively[8].

$$2H_2O + 2e^{-} \rightarrow H_2 + 2OH^{-} \quad \textbf{Eq. 6}$$

Some work has been done to limit hydrogen production in zinc air cells. Additives like lead and antimony have shown promise but are limited by their toxicity[8]. Zincate ions reduce the activity of water which in turn reduces the rate of hydrogen evolution[11]. Nafion has been explored as a coating on Zn particles, serving to keep zincate concentration high around the solid metal. When coupled with ZnO, KF and K_2CO_3, additives which reduce Zn oxidation and anode shape change, Nafion

coating on electrodes has been shown to increase the cycle life of the batteries[11].

The anode side of zinc air cell can be designed as either a flow battery, wherein electrolyte and zinc slurry are circulated through the cell, or with a stationary zinc anode. The flow design of the zinc anode has been shown to improve the morphology of zinc deposited during cell charging and allows for the removal of gases and remediation of the electrolyte outside of the cell[12]. Stationary zinc anode designs are inherently simpler than the flowing anodes, requiring less auxiliary equipment and avoiding issues such as shunt current. However, dendrite formation in deposited zinc during recharging can cause short circuiting within the cell.

1.1.3 Cathode

Oxygen from the air reacts at the triple phase boundary between oxygen, electrolyte, and solid catalytic surfaces in the cathode, illustrated in Figure 1. During discharge the oxygen is reduced, consuming the electrons liberated from zinc oxidation at the anode. This reaction is given in Eq. 7.

$$\frac{1}{2}O_2 + H_2O + 2e^- \rightarrow 2OH^- \qquad \textbf{Eq. 7}$$

The oxygen reduction reaction is sluggish, and a great deal of research effort is focused on catalyzing this reaction. There are two possible pathways for the reaction to occur, a less efficient two electron pathway, or a more efficient four electron pathway. Platinum group metals are proven catalysts that enable oxygen reduction along the four electron pathway, but their high cost has led to exploration of alternative catalysts. The air cathode can account for as much as 50% of the cost of a

zinc – air cell[13].

The cathode must be designed to allow oxygen to diffuse to the catalyst layer while preventing electrolyte from invading the pore space and hindering oxygen diffusion. Utilizing oxygen from air, while convenient and cost effective, introduces a challenge because oxygen concentration is air is ~20% and even lower if the air is fully humidified, so the mass transfer driving force is relatively low.

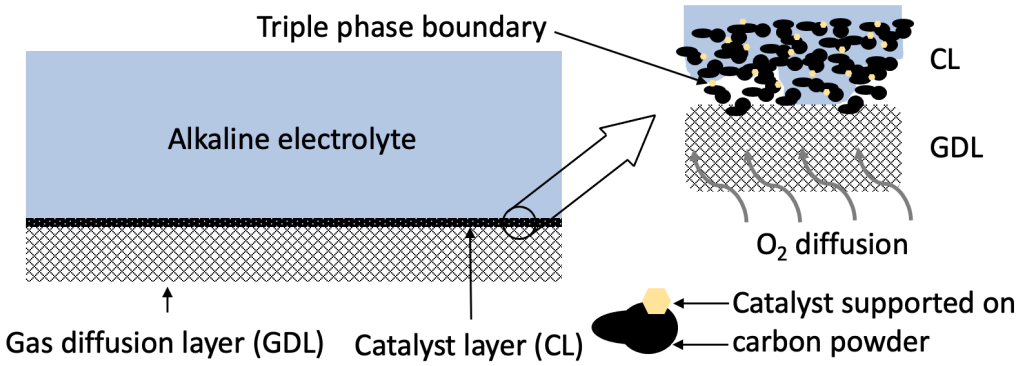

Figure 1 A digram of standard commercial cathodes used in zinc air batteries

Typical gas diffusion layers for the air cathode are composed of a carbon powder such as AB-7 (S_{BET} ~49m^2/g) and a hydrophobic binder, usually PTFE. The catalyst layer is similarly composed of a catalyst supported on carbon with a PTFE binder, though optimizing the electrochemically available surface area is critical to increasing the power density of the cell. Expanded nickel meshes are the most common current collector material. Nickel foams are sometimes preferred for their high surface area, and nickel coated copper mesh may be used to reduce material costs[13].

1.2 Objectives

The primary objective of this work is to produce novel gas diffusion electrodes

(GDEs) with improved mass transport properties for zinc – air batteries by electrospinning and electrospraying techniques. Typical cathode materials used in commercial zinc-air batteries consist of powder-binder composite gas diffusion layers with catalyst layers applied using a doctor blade technique, air spraying, or drop casting[14], [15]. Electrospun fiber mats offer higher porosity and larger pore sizes than powder composite materials, improving the mass transfer of oxygen to the catalyst by avoiding diffusion in the Knudsen regime. Electrospraying has been shown to produce electrode materials with favorable morphology, increasing power density of a cell[16][17].

Electrospinning enables the production of large amounts of nanoscale fibers. When randomly oriented and layered on top of each other these fibers form a highly porous material, exceeding 90% void space[18]. The technique is tunable; a few easily controllable parameters can be manipulated to target specific fiber properties that define the microstructure of the fiber mat[19]. Electrospraying techniques operate under similar principles to electrospinning and enable one to apply an amorphous porous layer to a substrate. The technique has been studied, particularly for catalyst layer application in PEM fuel cells, and has been shown to allow controllable catalyst loading producing catalyst layers with favorable mesoporous structure, high electrochemical surface area, and even catalyst distribution[17].

1.3 Outline of thesis

The work contained in this thesis explores novel cathode materials for zinc-air batteries that aim to improve performance by promoting mass transfer of oxygen and

increasing the electrochemical activity of the catalyst layer. Electrospun fibers were developed as a gas diffusion layer material so that their high porosity and large pore size may be taken advantage of. Electrospraying techniques were used to apply catalyst layers to the produced GDL materials as they have been shown to produce porous layers with a higher electrochemical activity than catalyst layers applied by conventional processes.

Chapter 2 provides an overview of energy storage technologies and demonstrates where zinc air batteries fit into the landscape. It then goes on to discuss some of the work that has been done in developing the air cathodes for zinc air batteries. A literature review of recent relevant research in developing electrospun and electrosprayed materials for zinc air batteries is also contained in this section.

Chapter 3 explains the experimental techniques used to produce and characterize the cathode materials produced in this work. The performance and characterization results for those materials is then presented in Chapter 4. The results section is structured to first give the reader an overview of the complete cathode materials studied, then presents the characteristics of each component in the cathode. The electrochemical performance of the materials produced in this work is the final section of this chapter. A summary of the results and discussion of their implications may be found in Chapter 5, as well as recommendations for further work.

2 Background and literature review

2.1 Energy storage and the case for zinc – air batteries

Large scale energy storage serves many purposes, but its greatest role is in integrating renewable sources of electricity into the existing grid infrastructure. Wind and solar power generation are the two largest sources of renewable energy that require energy storage. Behind hydroelectric and biomass generation, wind and solar are the 3rd and 4th largest producers of electricity, and are both limited in that their production rates vary with season, weather, and time of day[20]. The intermittency of renewable electricity causes several problems. Taking the long view, it means that, without effective storage technologies, renewable electricity can never completely replace conventional electricity generated from thermal energy.

To ensure efficient utilization of low carbon energy, renewables are given priority in the grid and are distributed to match production rates; conventional electricity producers are required to modulate their energy output, accommodating the renewable producers. This is inefficient from a cost and thermodynamic standpoint as thermal generators must be brought on and off line more frequently[21]. Energy storage, in its many different forms, helps to smooth the temporal fluctuation inherent in renewable electricity, easing grid integration. The marginal benefit of energy storage is a function of the difference in cost between intermittent and reliable sources of energy. Losses incurred by the storage technology must be taken into account[22].

When considering how to store electricity one is faced with two options,

accumulating the electrons directly and drawing upon them when required, or transforming the electrical energy into a different form for storage, such as potential energy, then converting back to electrical energy as desired. The former is termed direct energy storage and, though efficient, direct energy storage technology requires much more development to be viable at large scale. Indirect energy storage, which is farther along in development and adoption, and can be subdivided into, mechanical, thermal, and electrochemical energy storage. Uninterruptable power supplies (UPS) improve power quality at the grid scale and require technology that can provide electricity almost instantaneously. Transmission and distribution (T&D) challenges, such as integrating large amounts of renewable power during peak production, are addressed by energy storage technologies that have a larger energy capacity and higher power rating.

Pumped hydroelectric (PHES) and compressed air energy storage are both examples of mechanical storage technology, with PHES accounting for 99% of the energy storage capacity in 2010[23]. Their high-power rating and large energy capacity make them suitable to handle large changes in electricity demand, but they are unsuitable for short duration applications and are limited geographically by the location of suitable reservoirs.

The T&D benefits of electrochemical energy storage has generated interest in developing grid scale battery technologies that improve the power quality of existing infrastructure and enable the large-scale integration of renewables. Metal – air batteries seem particularly well suited to meet this need. Because the cathodic reaction utilizes atmospheric oxygen they offer higher specific energy than lithium-

ion batteries and are more flexible than conventional batteries in that power and energy storage may be decoupled [24].

Zinc – air batteries in particular have received a lot of interest as a large-scale energy storage technology, primarily for safety and economic reasons. Zinc is an abundant, easily recyclable metal that is stable in solution[8]. Though the theoretical specific energy of other metals, such as lithium or aluminum, is higher than zinc, they are either unstable in solution or readily corrode necessitating further development to overcome these challenges[24].

That is not to say zinc – air battery technology is fully realized; a number of problems must be solved before its potential for large scale energy storage can be fully realized. Designing electrically rechargeable zinc – air batteries is proving quite challenging. Catalysts are required for the oxygen evolution and reduction reactions that occur during cell charge and discharge. Optimally catalyzing these reactions have proven to be one of the biggest challenges zinc air batteries face. To avoid recharging issues primary zinc air batteries where the anode is replenished with fresh zinc, are being developed.

2.2 Cell performance analysis

One of the most common experiments to understand the electrochemical performance of batteries and fuel cells is to measure the deviation from open cell voltage that occurs when the current flow increases. Taking multiple current measurements at different operating voltages and plotting voltage against current produces a “polarization curve”.

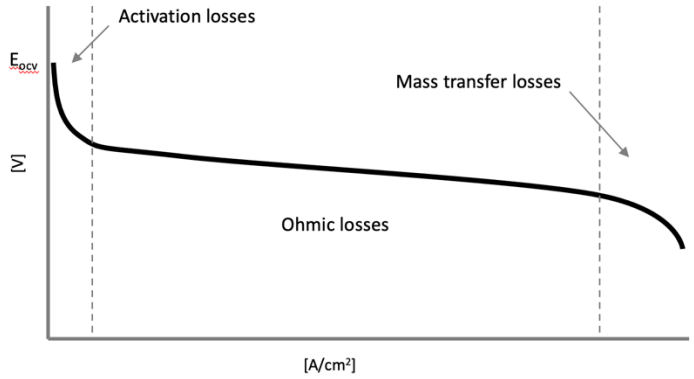

Figure 2 A general sketch of a polarization curve

Generally, potential losses occur in three different regimes. Activation losses occur at low current densities and are due to the electrochemistry of the cell. Sluggish reactions with high activation energy have more activation potential loss than reactions with fast kinetics. As current density increases ohmic losses govern the system. Ohmic losses follow Ohm's law, where the resistance is the internal resistance of the cell. These losses are caused by the resistance of the electrodes and electrical connections within the cell as well as resistance to ion flow in the electrolyte. Ohmic losses can be managed though cell design. Reducing the space between the anode and cathode, for example, reduces potential losses in the electrolyte. At high current densities reactions are proceeding as fast as possible at the anode and cathode, so fast that reactants can't reach the active sites to keep pace with the reaction and mass transfer losses are incurred. In zinc air batteries mass transfer losses are incurred at the air cathode as oxygen must diffuse though the cathode to triple phase boundaries at active sites to participate in the reaction[25].

2.3 Air cathode design and research

The significance of the mass transport properties in zinc-air cathode performance becomes apparent when studying degraded cathodes where hindered mass transport leads to a reduction in cell performance. In 2015 Ma et al investigated degradation phenomena in zinc air cathodes by comparing electrochemical and mass transport performance of new and used cathodes, supporting the results of their characterization work with SEM imaging [26]. Little information was given about the condition of the used cathodes, other than being "seriously degraded".

Comparing the polarization curves of the new and used cathodes showed a clear reduction in performance; polarization experiments showed that the peak power density was reduced by almost 40% for the used materials[26]. The early onset of mass transfer losses in the used cathode materials suggests that reduction in oxygen transfer as the cell ages is the cause for the reduced performance while EIS experiments conducted with the new and used materials produced spectra that suggest both a reduction in mass transport and electrochemical activity for the used cathode.

SEM images of the used cathode materials in the Ma et al paper showed a reduction in pore space in the catalyst layer as well as a reduction in nanoscale roughness. Both changes reduce electrochemical area, decreasing the power density of the cathode. The gas diffusion layer of the used material also showed signs of degradation; SEM images revealed a reduction in micropores and pressure drop was greater across the used cathode material as a result of these changes [26]. Their work showed that the primary causes for reduced battery performance were degradation

of the both the gas diffusion layer and the catalyst layer, impairing mass transfer and electrochemical activity.

The electrochemical reactions in the air cathode occur at the triple phase boundary, where liquid electrolyte meets solid catalytic surfaces and gaseous oxygen. Yu et al have recently published work wherein they explore improving reaction rate at the cathode by increasing the triple phase boundary. In their work they treated one side of a carbon fiber paper with PTFE and grew a nickel iron layered double hydroxide (NiFe-LDH) catalyst on the opposite, untreated, surface[27].

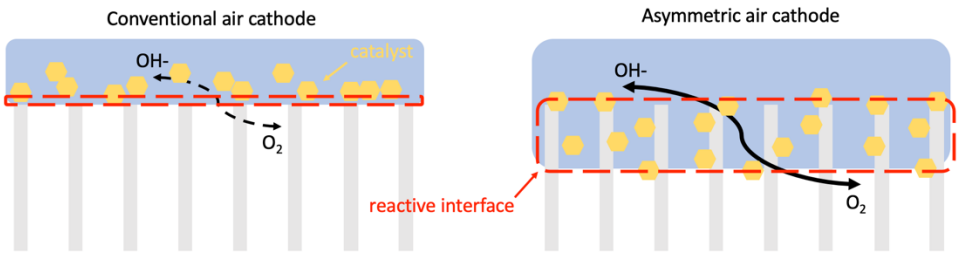

Figure 3 Schematic of the asymmetrical air cathode design developed by Yu et al [27]

This asymmetrical cathode design promoted greater electrolyte penetration into the catalyst layer than conventional zinc - air catalyst layers that use a PTFE binder. The asymmetrical material performed better than the conventionally designed cathode exhibiting less voltage loss with increasing current density and better cyclability, which the authors attribute to the increased triple phase boundary[27].

Optimizing oxygen transport to the catalyst layer is also an important consideration in air cathode design, though it has received less focus than catalyst

layer development. Xu et al worked on optimizing the gas diffusion layer properties in cathode materials composed of a nickel foam, serving as both a current collector and MnO_2 catalyst support, and a PTFE and carbon nanotube GDL. By adjusting the PTFE:CNT ratio they were able to tune the hydrophobicity and oxygen transport of the gas diffusion layer[28]. They determined a PTFE:CNF ratio between 1:2 and 1:4 to be optimal for several reasons. The 1:2 GDL was shown to contain more micropores with diameters below 5 nm. The authors attribute this to an increase in mass transport. Additionally the 1:2 material had the highest BET surface area of all cathodes studied, due to the PTFE acting as a spacer between CNT groups, modifying the pore structure to encourage oxygen diffusion[28].

Wang et al also explored tailoring the pore size and properties of the gas diffusion layer, but rather than adjusting the PTFE:CNT ratio they grew Co_3O_4 nanosheets on a carbon nanotube and nickel foam substrate. The Co_3O_4 nanosheets served as electrocatalysts while also modifying the pore structure of the GDL to promote oxygen diffusion[29]. Intrinsically Co_3O_4 has poor conductivity, however this was mitigated by growing the nanosheets directly on the nickel foam. The material with Co_3O_4 nanosheets featured more nanopores with diameters below 5nm which allowed for increased oxygen diffusion while maintaining the requisite hydrophobic properties.

Compared to a control material with a conventional platinum catalyst supported on carbon, the Co_3O_4 nanosheet electrodes resulted in a higher power density, improved ORR performance, and superior cycle stability. The power density can be attributed to both the improved oxygen transport and increase in electrochemical

surface area, both results of the unique Co_3O_4 nanosheet structure.

2.4 Electrospinning of fibrous mats

Another approach to improve oxygen transport to the catalyst layer is by using electrospinning techniques to produce GDLs with nanoscale fibers and high porosity. The many advantages of these materials are related to their "goldilocks" pore sizes, large enough to avoid Knudsen diffusion and small enough to limit water invasion.

Electrospinning is a polymer processing technique that allows high aspect ratio fibers to be produced with relative ease. "Electro" refers to the difference in electrostatic potential that draws the polymer solutions into fibers. Polymer solution is pumped to a needle tip some distance from a collector surface. The potential difference between the polymer and collector causes a jet of polymer to travel through the air to the collector. At the needle tip, the polymer solution forms a conical shape, referred to as a Taylor cone.

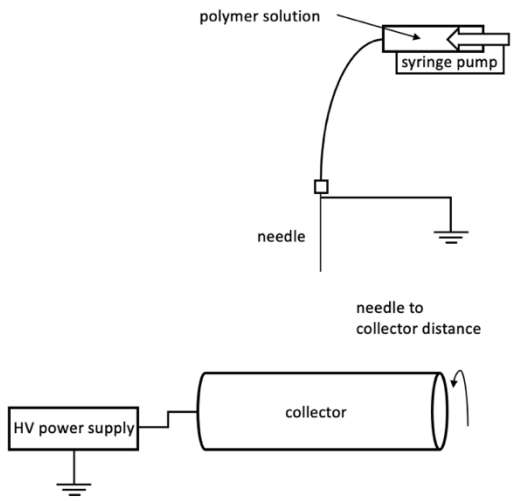

Figure 4 An sketch of the components of an electrospraying apparatus, showing the equipotential lines between the needle and collector[30]

As the jet travels from the Taylor cone to the collector whipping instability occurs. The polymer jet experiences rapid whipping motion and large shear forces reduce the jet diameter. Solvents are driven off before the polymer reaches the collector where thin randomly oriented fibers accumulate, forming a porous mat[31]. Polyacrylonitrile (PAN) is commonly electrospun as a precursor to carbon fibers, as it produces stable, high purity carbon fibers with relative ease and high yield [32].

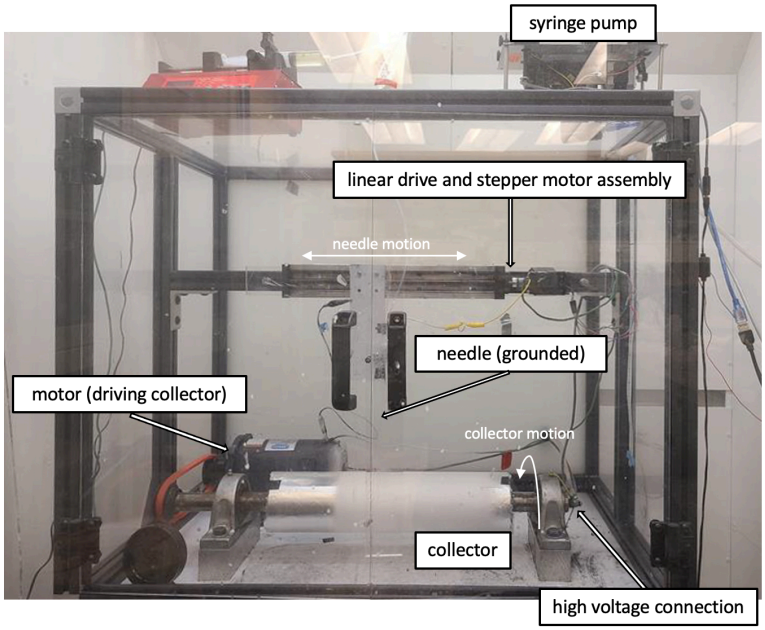

Figure 5 A labeled image of the electrospinning apparatus used in this work

2.5 Carbonization of electrospun materials

Carbon fibers are produced from PAN fibers by a multi-stage carbonization process. The first stage in the carbonization process is commonly referred to as the stabilization stage and takes place under an air atmosphere between 200 and 300°C. During the stabilization stage cyclization and dehydrogenation reactions occur simultaneously and the linear structure of PAN is converted into a heterocyclic

structure [33]. This ladder-like structure can withstand the high temperatures of the subsequent carbonization stage. The degree that the cyclization reactions proceed during the stabilization stage has been shown to have an effect on final properties of the carbon fibers, such as conductivity and fiber strength[34].

Carbonization is typically carried out between 800 and 2000°C under an inert atmosphere such as nitrogen or argon gas. During this process non-carbon elements, namely nitrogen, hydrogen, and oxygen are driven off, resulting in a high purity carbon fiber. It has been shown that as carbonization temperature increases graphitic carbon content increases and conductivity improves, while heteroatom content decreases[33].

2.6 Electrospraying of porous films

Electrospraying is a technique similar to electrospinning, but rather than producing long fibers from a polymer solution, electrospraying atomizes a solution of solid particles dispersed in a solvent. The atomized solution is drawn from the Taylor cone to the collector surface in the same manner as in electrospinning, and solvent is driven off during the process. The particles deposited by electrospraying have been shown to produce porous layers with a fractal structure and high surface area, favourable characteristics for catalyst layers[17].

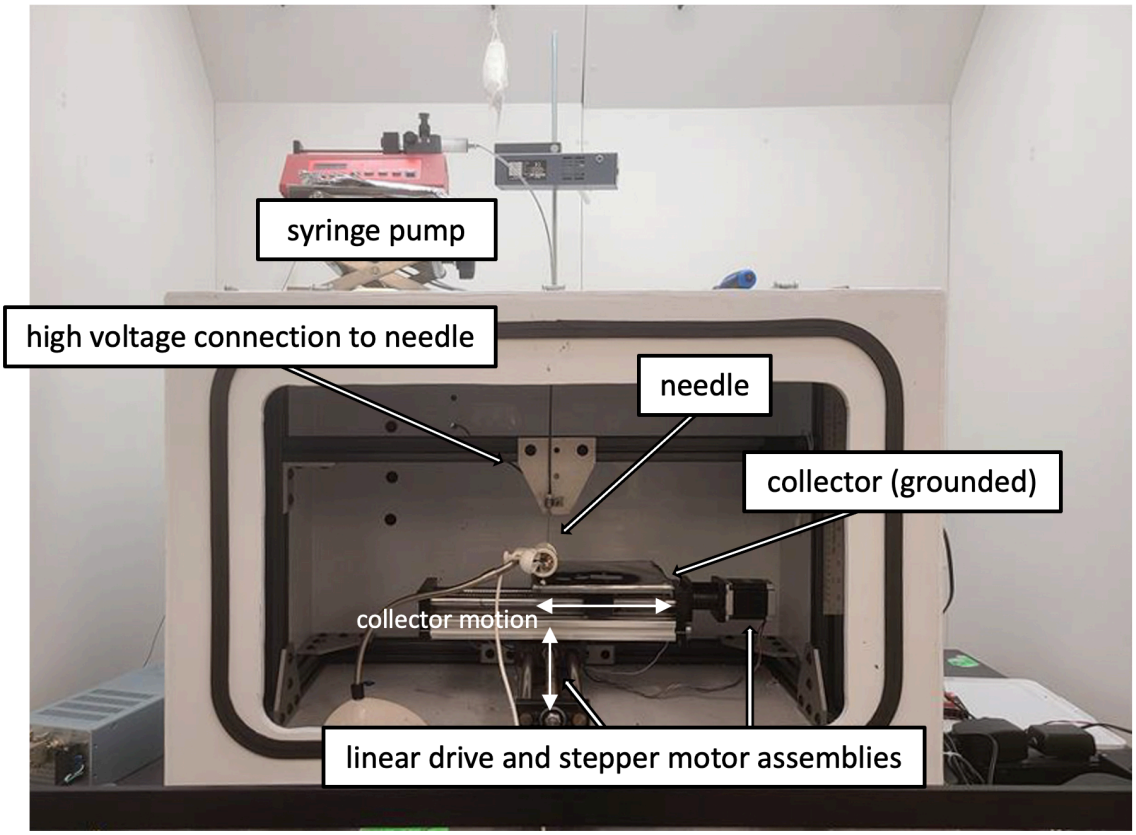

Figure 6 A labeled image of the electrospraying apparatus used in this work

2.7 Electrospinning and electrospraying to produce air cathodes

As recently as the early 2000's, electrospinning research was concerned with understanding the experimental parameters and morphologies achievable with electrospinning techniques. More recently, focus has shifted to creating functional electrospun fibers. Electrospun fibers with embedded catalysts, for example, are relatively easy to produce by including metal salts in the PAN/DMF solution. These salts serve as precursors to electrochemically active metal and metal oxide inclusions that form in the fibers during carbonization. Electrospun materials have been utilized in zinc air cathode design in other manners, though the majority of the focus has been on developing catalytically active fibers[16]. The interest is driven by the high cost of

conventional catalysts such as platinum and iridium.

Lanthanum cobalt oxide has been successfully integrated into electrospun carbon fibers by Shim et al; they produced porous carbon fibers with $LaCoO_3$ inclusions by incorporating lanthanum and cobalt salts into the electrospinning solution[35]. $LaCoO_3$ formed during carbonization of the fibers, developing pore space in the fibers at the same time. These electrochemically active fibers were then incorporated into a catalyst layer with a PTFE binder. Though the $LaCoO_3$ catalyst did not outperform conventional PGM catalysts, the catalysts supported on electrospun fibers did perform better than $LaCoO_3$ in powder form.

The electrospun fibers with integrated catalysts were also found to have a higher BET specific surface area than the powder catalysts, 5.43 m^2/g compared to 4.54 m^2/g [35]. The authors attribute the increased electrochemical activity of the electrospun materials to a greater availability of active sites.

Higher specific surface areas increasing the effectiveness of catalytically active electrospun carbon fibers is a common trend in research developing electrospun materials for zinc – air batteries. Park et al have developed high surface area electrospun fibers with a "churros" morphology by electrospinning homogenous solutions of PAN and polystyrene (PS)[36]. Differences in surface energy between the PAN and PS cause microphase separation within the electrospun fiber. During carbonization the PS decomposes creating a highly porous inner structure of channels oriented along the fiber axis. These fibers had a high specific surface area, 1271.2 m2/g, and contained electrochemically active nitrogen-carbon heteroatoms.

Similar to the $LaCoO_3$ study, these fibers were incorporated into a catalyst layer

and applied to a gas diffusion layer, rather than kept in a free-standing sheet. They demonstrated good ORR performance, with an n value of nearly 4, indicating that they promote the ORR reaction along the ideal four electron pathway[36].

While the bulk of the work in developing electrospun materials for has focused on catalyst layer design there has been some development of free standing electrospun fiber sheets for zinc air battery applications. Huang et al explored electrospun polystyrene (PS) and polyethyleneimine (PEI) sheets to absorb CO_2, preventing the formation of carbonate and other compounds that have been shown impair performance of zinc air cells[37]. The amine groups in the PEI polymer have good CO_2 absorbent properties and can be regenerated by heating the fibers to 70°C. Performance testing of a zinc air cell with and without the electrospun membrane showed an increase in discharge capacity, from 762 mAh/g to 801 mAh/g with the membrane at a current density of 10 mA/cm^2[37]. Other architectures of CO_2 adsorbing electrospun fibers have been investigated. Zainab et al developed an electrospun structure with "nanonets" of PEI that offer improved mechanical properties over the purely fibrous materials [38].

There has been very little work in developing electrosprayed catalyst layers for zinc air batteries. Ahmad et al have used electrospraying techniques to apply cathode layers of highly durable iron particles encapsulated in graphitic carbon[39]. But their research was primarily focused on development of alternative, lower cost catalysts as opposed to electrospraying techniques. Application of PEMFC catalyst layers by electrospraying has received much more attention. Dendritic structured catalyst layers with lower resistivity and larger active electrochemical area have been

produced by electrospraying and show promise as a means to reduce catalyst loading requirements, reducing the cost of a cell [17], [40]. Conventional catalyst layers for PEMFC cells use platinum on carbon as a catalyst and Nafion as a binder and conductor of hydroxyl ions, while catalyst layers in zinc air cells are currently using platinum on carbon with a PTFE binder.

3 Experimental techniques

3.1 Chemicals

The fibers produced in this study were electrospun from solution of PAN dissolved in DMF. Fiber surfaces were coated with PTFE, a hydrophobic fluoropolymer that is also known by its product name, Teflon. Inks used to create the electrosprayed layers were composed of a powder, a PTFE dispersion, and solvents. Chemicals used to produce GDE materials are listed in Table 2 while chemicals used for material characterization are included in Table 3.

Table 2 Chemicals used in material production

	Compound	Relevant Properties	Supplier
Electrospun Fibers	N,N-Dimethylformamide	Purity: 99.8%, anhydrous	Sigma Aldrich
	Polyacrylonitrile	Avg. Mw: 150,000 g/mol	Sigma Aldrich
Fiber Coating	Teflon DISP 30	Solid Content: 60wt%, Particle Size: 220nm, Melting Point: 337°C	Fuel Cell Store
Microporous Layer	Vulcan XC72R	Particle size: 50nm, BET surface area: 235 m2/g	Fuel Cell Store
	Teflon DISP 30	Solid Content: 60wt%, Particle Size: 220nm, Melting Point: 337°C	Fuel Cell Store
	Ethanol	.10% water maximum	Chem Stores
	Deionized Water		
Catalyst Layer	Platinum on carbon	40wt% Pt on Vulcan XC-72R	Fuel Cell Store
	Teflon DISP 30	Solid Content: 60wt%, Particle Size: 220nm, Melting Point: 337°C	Fuel Cell Store
	Nafion dispersion D2020	20wt% Nafion, 34% water, 46% alcohol	Fuel Cell Store
	Ethanol	Absolute, .10% water maximum	Chem Stores
	Deionized Water		

Table 3 Chemicals used in material characterization

	Compound	Relevant Properties	Supplier
Porosity	Flourinert FC-3283	Density: 1.82 g/ml	3M
DVS Adsorption	Cyclohexane, Laboratory reagent ≥ 99.8%	Molecular cross section area: 39 $Å^2$	Honeywell
Radial Diff	Nitrogen Gas		
	Air		
Test Cell	Potassium Hydroxide, ACS reagent ≥ 85%		Sigma Aldrich
	Zinc dust, ≥ 98%	Particle size: ≤10μm	Sigma Aldrich

3.2 GDE material production

3.2.1 Controlling fiber morphology (diameter, shape, range of fiber sizes)

The working parameters that have the most significant effect on fiber diameter are concentration of the polymer in the electrospinning solution and the distance between the collector and the Taylor cone[41], [42]. Fiber diameter has been shown to decrease with polymer concentration, to a critical "crossover" concentration, below which the solution is not spinnable.

The ability to electrospin a polymer solution largely depends upon the degree of interaction between polymer chains in solution. These solutions can be conceptualized as having two distinct regimes, with the transition between the two occurring at c*, the critical concentration[43]. Below the critical concentration polymer interaction does not occur appreciably and the solution is not electrospinnable[43]. The critical concentration depends on the average molecular weight of the polymer, chain flexibility, temperature, and solvent-polymer interactions. Eq. 8 relates the critical concentration to the molecular weight (M) the root mean square end to end distance ($<r^2>$) of the polymer[44].

$$c^* = \frac{3M}{4\pi\langle r^2\rangle^{3/2} N_A} \qquad \textbf{Eq. 8}$$

As the concentration is increased beyond c* chain entanglement increases and spun fiber morphology transitions from fibers with large diameter sections (beads) to a consistent cylindrical shape with little variation in fiber diameter[43].

As the distance between the needle tip and collector increases the jet radius decreases due to stretching caused by the electrostatic force on the solution and whipping instability as the jet travels from the Taylor cone to the collector. There is a theoretical terminal jet diameter, the smallest jet diameter caused by whipping instability[45]. If the distance from the needle tip to the collector is not great enough to allow the terminal jet diameter to be achieved the spun fibers will not have reached the smallest diameter when they reach the collector. The needle to collector distance used in this work was 15cm to allow for the terminal jet diameter to be achieved.

The values for the other operating parameters used to electrospin PAN fibers in this work were essentially defined by what allowed the solution to be electrospun continuously without polymer solution dripping from the needle. The flow rate of solution to the needle tip and potential difference between the collector and polymer solution was set such that the amount of polymer solution entering and leaving the Taylor cone was at steady state. Humidity has been shown to effect fiber morphology as well as the mechanical properties of the fiber mat[46] and high relative humidity causes partial phase separation, forming a skin on the outer surface of the Taylor cone, resulting in solution dripping rather than spinning. To address this issue nitrogen was used to displace high water content air in the electrospinning apparatus.

3.2.2 Electrospinning

PAN fibers were electrospun from a PAN/DMF solution on a custom-built apparatus consisting of a Cole-Palmer syringe pump, 10 cm diameter collector drum, and a Glassman, MJ30N0400-11 high voltage power supply. The drum was coated in aluminum foil, the substrate that the PAN fibers were deposited onto. A grounded 18-gauge needle was positioned 15cm above the collector drum. Voltages between 15 and 21kV were applied to the drum, establishing a potential difference between the needle and collector. The needle was rastered left and right, along the long axis of the collector drum at a speed of 5mm/s, coating the surface of the drum, creating a rectangular sheet of electrospun fibers on the aluminum foil substrate.

3.2.3 Carbonization

An MTI GSL-1700X tube furnace was used to carbonize the electrospun PAN fibers. There is a great deal of work in optimizing the carbonization process [33][34][47], and the temperature profile used to carbonize the electrospun fibers, Figure 7, is based on this work. Sheets of PAN fibers were sandwiched between two 8 cm by 16.5 cm graphite plates and loaded into the furnace, allowing sheets of carbon

fibers with a maximum size of 13 by 6.5 cm to be produced.

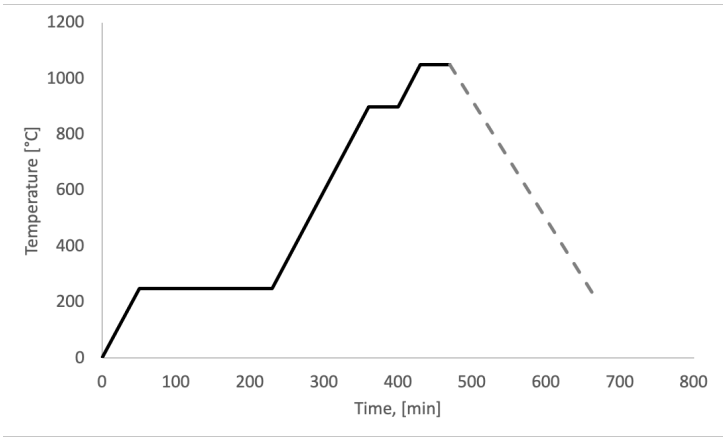

Figure 7 The temperature profile used for carbonization

The temperature profile used features three constant temperature stages at 250°C, 900°C, and 1050°C. Between stages the heating rate was set to 5°C/min. After the final stage the furnace was cooled at a controlled rate to below 200°C, at which point the heating element was turned off and the furnace cooled to ambient temperature uncontrolled.

A flow line with an analog gas flowmeter was ported into the front cap of the furnace. After 2 hours and 50 minutes had elapsed (2 hours into the 250°C stabilization stage) nitrogen flow was turned on at 150 sccm, displacing air in the furnace with an atmosphere of inert gas.

3.2.4 Teflon coating

Bare carbon fiber mats were made hydrophobic by coating the fiber surface with PTFE. A solution of DISP 30, a PTFE dispersion, and water was made and forced

into the porous fiber mats under a ~93 % vacuum (approximately 28 in. Hg below atmospheric pressure). The concentration of the PTFE/water solution was such that the desired amount of PTFE loading would be achieved when the material was completely saturated. In addition to the hydrophobic properties of PTFE, the difference between the melting temperature (327 °C) and ceiling temperature (650 °C) lends the polymer to melt processing techniques, such as the one used in this work.

After the PTFE solution had been forced into the GDL materials, the sheets of saturated fibers were dipped into deionized water once, to remove excess PTFE solution from the surface of the sheets. The treated samples were then left to dry at ambient conditions for 12 hrs, before sintering the PTFE loaded material in a tube furnace. Figure 8 is the temperature profile used to sinter PTFE loaded materials. The 120°C, 270°C, and 337°C stages are recommended by the manufacturers of DISP 30 and serve to evaporate water, drive off dispersing agents, and melt the PTFE, respectively. The furnace is cooled at a controlled rate from 337 to 200°C.

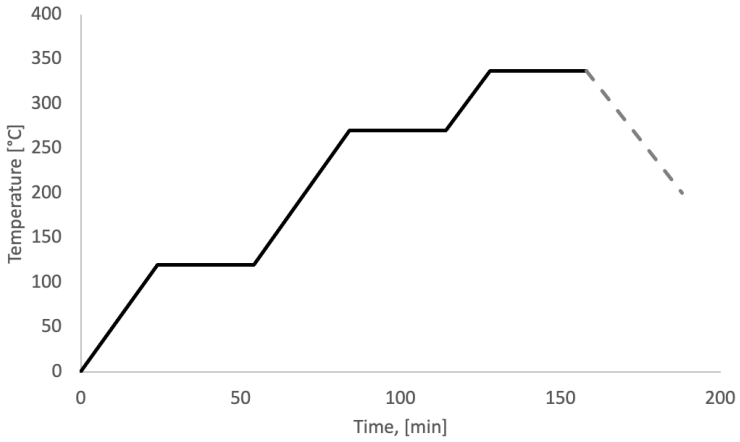

Figure 8 The PTFE sintering temperature profile used in this work

3.2.5 Electrospraying

The same electrospraying apparatus was used to apply the microporous and catalyst layers to the surface of the electrospun gas diffusion layer materials. The device consisted of stationary needle charged by an MJ series Glassman power supply. The electrospraying solution, commonly referred to as ink, was fed to the needle by a New Era syringe pump, model NE-1010. The collector was positioned below the needle; unlike the electrospraying apparatus drum, the collector was a flat stainless-steel plate, connected to ground. Stepper motors connected to lead screws enabled the collector to be moved in the x and y direction below the needle so that rectangular spray patterns were possible.

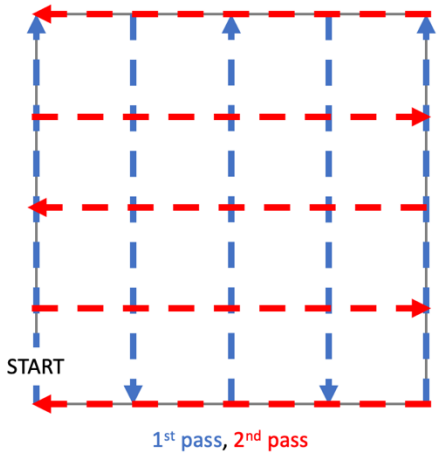

Figure 9 Electrospraying pattern used to apply MPL and CL.

The syringe pump, power supply, and collector plate movement were all controlled by a LabVIEW VI. An Arduino Uno and two stepper motor drivers were used to send power to the stepper motors.

3.2.6 Electrospraying the microporous layer

The ink for the electrosprayed microporous layer was composed of Vulcan XC72R carbon powder and DISP 30. Water and ethanol in a 1:1 ratio were used as solvents to dilute the ink to a concentration of 2.5 mg carbon per millilitre of solution. PTFE loading in the MPL was designed to be 50wt%, the same as the reference material. Sonication for at least 60 minutes was necessary to achieve good dispersion of solids in the ink. The MPL ink was sprayed from a distance 5.5cm above the collector plate using an 18-gauge needle. The flowrate was .5 ml/hr and a voltage of 5.5kV was applied to the needle. 40 loops were made to achieve a uniform MPL layer, with an average loading of .27 mg/cm2 and a thickness of .014mm. Once applied, the MPL was sintered using the temperature profile illustrated in Figure 8.

3.2.7 Electrospraying the catalyst layer

Two electrosprayed catalyst layers were developed in this work, both using 40wt% platinum on Vulcan XC-72R carbon powder as a catalyst. The inks were designed to have a solid fraction of 2.5mg/ml to insure good dispersion in the solvent. Similar to the MPL ink the solvents used were water and ethanol in a 1:1 ratio. In one ink a PTFE loading of 25wt% was achieved by including the appropriate amount of DISP 30 to the ink. The second catalyst layer design used Nafion as a binder at a loading of 30wt%.

Both inks were electrosprayed on the same apparatus used for MPL application using a 22-gauge needle. The distance from the needle tip to collector surface was 5.5 cm. A flowrate of .7ml/hr was used with 5.9kV applied to the needle. After

electrospraying the PTFE catalyst layer was sintered while the Nafion catalyst layer was used as is. Both layers were applied to achieve a catalyst loading of .4mgPt/cm^2.

Catalyst loading was calculated by taking the difference between the electrode mass before and after catalyst layer application, dividing by the surface area for the electrode material, and then calculating the mass of platinum per cm^2 using the composition of solid components in the catalyst layer ink, demonstrated in Eq. 9.

$$\left(\frac{\text{mass difference, g}}{\text{electrode area, cm}^2}\right)\left(\frac{.75\text{ g catalyst}}{\text{g ink solids}}\right)\left(\frac{.4\text{ g Pt}}{\text{g catalyst}}\right) \qquad \textbf{Eq. 9}$$

3.3 Characterization

3.3.1 SEM

Scanning electron microscopy (SEM) was used to determine fiber geometry as well as the morphology of electrosprayed layers. SEM images also provided some qualitative insight into the PTFE distribution on the fiber surfaces. A Quanta FEG 250 instrument was used to obtain the images, and the Fiji distribution of ImageJ software was used to measure fiber diameters. Multiple measurements were made on several images (at different locations) for each sample, allowing for an average value and standard deviation of fiber properties to be obtained.

3.3.2 Specific surface area

The specific surface area of the porous materials produced in this work was determined by BET analysis of adsorbed cyclohexane. The isothermal adsorption experiments were conducted using a DVS Resolution instrument, produced by Surface Measurement Systems. The high resolution of the balance in this instrument, used to

measure gas adsorption, allowed for the relatively low specific surface area fiber materials to be measured without requiring a large sample mass.

BET theory has become a standard technique to estimate the specific surface area of a material from an isothermal adsorption experiment. An adsorption experiment produces a dataset of the specific amount of adsorbate that adsorbs onto the adsorbent, *n*, at some relative pressure, P/P_o. Plotting experimental data according to a linear form of the BET equation, Eq. 10, allows one to calculate the number of molecules adsorbed in the first layer, n_m [mol/g], and the BET constant, *C*, from the slope and y-intercept of line of best fit. If the cross-sectional area of the adsorbate is known, the specific surface area may be calculated from n_m[48].

$$\frac{P/P_o}{n\left(1 - P/P_o\right)} = \frac{C-1}{Cn_m}\left(P/P_o\right) + \frac{1}{Cn_m} \qquad \textbf{Eq. 10}$$

Misleading specific surface answers can be produced by BET theory, especially for microporous materials [49]. Measures were taken to ensure that the data used in BET analysis agreed with all criteria put forth by Rouquerol et al., and the specific surface area answers reported in this work are the highest values produced by a relative pressure range that agrees with the BET isotherm model. Because the mass fractions of each layer (GDL, MPL, and CL) were known, the specific surface areas of the layer could be calculated from the specific surface area of the total material.

3.3.3 Breakthrough pressure characterization

The pressure at which electrolyte is forced through the MPL into the GDL, flooding the cell and effectively blocking all oxygen diffusion to the catalyst layer is one of the most important performance metrics for cathode materials in metal air batteries. This pressure, the breakthrough pressure, was measured using an apparatus that was originally designed to evaluate the water saturation of gas diffusion layers as a function of capillary pressure [50]. Water was forced through the GDL sample from above by a New Era NE-1010 syringe pump while the pressure of the water being forced through the sample was monitored using an Omegadyne Inc. PX409-030A5V pressure gauge, shown in Figure 10. A saturated hydrophilic PES membrane with a .03 μm pore size was placed in the holder below the sample and a water filled flow line led from the sample holder to a reservoir on an analytical balance at atmospheric pressure. When completely assembled, the pore space of the sample is the only part of the system not saturated with water.

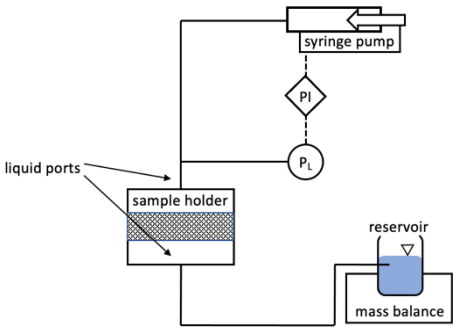

Figure 10 A diagram of the breakthrough pressure system design

Breakthrough pressure was achieved by increasing the differential pressure of water across the sample using a syringe pump. At breakthrough pressure water was forced though the material and water began to flow through the sample. This flow of water was detected by an increase in the mass of water in the reservoir.

The differential pressure and reservoir mass were measured and logged over time using a LabVIEW program. The datasets allow one to easily correlate the pressure at which the reservoir mass begins increasing, the breakthrough pressure.

Modifications were made to achieve pressures high enough to force water though the commercial backing layer. The syringe pump was replaced with a voltage controlled pressure regulator from Proportion-Air, model QB1SSFEE500. The higher pressures necessitated a pressure sensor with a higher range, so an Omegadyne Inc. model MMG250V10P1C0T4A6 sensor with a maximum pressure of 250PSIG was installed and the LabVIEW VI was adjusted accordingly. In this arrangement the cavity above the sample was loaded with water while the line connecting to the sample holder contained air. The air pressure above the water filled cavity was controlled by the pressure controller.

3.3.4 In-plane effective diffusivity and tortuosity

The effective diffusivity of oxygen in the in-plane direction was evaluated for both the electrospun and electrosprayed materials produced in this work using an analytical technique published by Kim et al. [51]. The experiment employs a radial, gasket free design, and technically measures the effective diffusivity in the radial direction.

Note that the electrospun GDL materials are anisotropic, meaning that the in-plane effective diffusivity is not equal to the through-plane effective diffusivity. For fibrous mats, one can visualize diffusion in the through-plane direction as diffusion layers of randomly cross-hatched fibers, while diffusion in the in-plane direction occurs in the same direction as the fiber axis. Through-plane values are understood to correlate to in-plane diffusivity values. Previous experiments on conventional gas diffusion layers used in PEM fuel cells have shown that in-plane diffusivity is consistently about two times higher than the through-plane value [52], [53].

The powder/binder composite materials and the electrosprayed layers produced in this work are isotropic, so their in-plane effective diffusivities found using this technique are representative of their through-plane effective diffusivities.

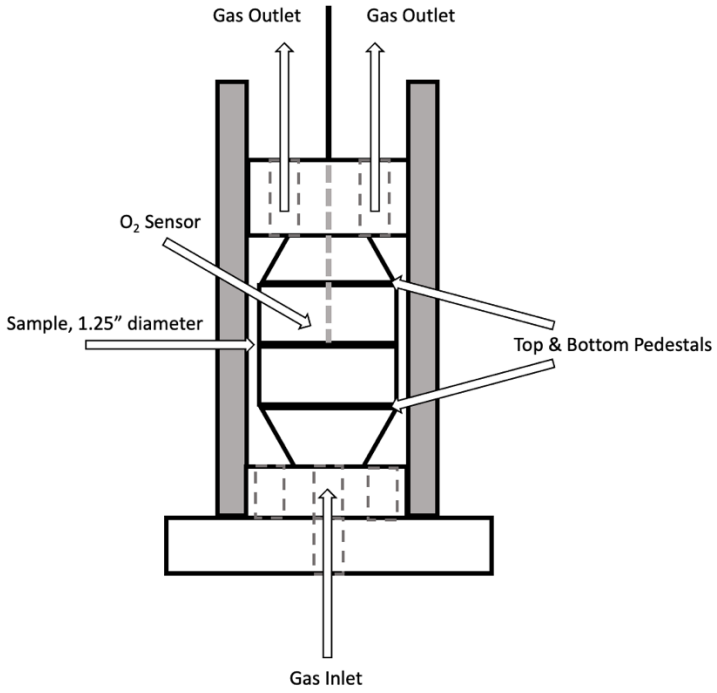

Figure 11 The apparatus used to measure effective diffusivity in this work

To measure the radial diffusivity of a material, a cylindrical sample is placed in-between the upper and lower pedestals, with the perimeter exposed for gases to diffuse through. Initially the oxygen concentration was 20.9%, for t > 0 the apparatus was flooded with nitrogen gas, reducing the oxygen concentration to 0%; these boundary conditions are given in Eq. 11. Nitrogen diffuses radially, towards the center of the sample, where oxygen concentration is measured with an OXR430-UHS fiber optic oxygen sensor and recorded over time.

$$C(t) = C_o \text{ at } r = R \text{ and } t = 0$$
$$C(t) = C_1 = 0 \text{ at } r = R \text{ and } t = 0 \qquad \textbf{Eq. 11}$$

Assuming that diffusion only has a radial component, Fick's second law in cylindrical coordinates, for some species "i", reduces to Eq. 12.

$$\frac{\partial C_i}{\partial t} = \frac{1}{r}\frac{\partial}{\partial r}\left(rD\frac{\partial C_i}{\partial r}\right) \qquad \textbf{Eq. 12}$$

The dataset generated in each experiment, of oxygen concentration at r=0 versus time, is fit to the analytical solution for the diffusion equation, Eq. 13 using the method of least squares and producing the diffusion coefficient, D_{eff} [54]. In Eq. 13 J_1 and J_0 are the zeroth and first order Bessel functions of the first kind.

$$\frac{C(t)-C_1}{C_0-C_1}=1-\frac{2}{R}\sum_{n=1}^{\infty}\frac{e^{(-D\alpha_n^2 t)}J_0(\alpha_n r)}{\alpha_n J_1(\alpha_n R)} \qquad \textbf{Eq. 13}$$

It is important to note that the D_{eff} provided by this technique differs from the concept of effective diffusivity widely used in porous media characterization. Typically, effective diffusivity in porous media is interpreted as:

$$D_{eff}=\frac{\varepsilon}{\tau}D_b \qquad \textbf{Eq. 14}$$

However, in this technique, the effective diffusivity value should be understood to be:

$$D_{eff}=\frac{1}{\tau}D_b \qquad \textbf{Eq. 15}$$

This is because in porous media diffusing species can only be in the pore space, so the transient term in the continuity equation for species must be scaled by the porosity, ε, in porous media, as shown in Eq. 14 [55]. Substituting the definition of D_{eff}, Eq. 14, into Eq. 16 cancels out the porosity term, and the resulting transient equation governing this experiment, Eq. 17[51].

$$\varepsilon\frac{\partial C}{\partial t}=D_{eff}\nabla^2 \mathrm{C} \qquad \textbf{Eq. 16}$$

$$\frac{\partial C}{\partial t}=\left(\frac{D_b}{\tau}\right)\cdot\nabla^2 \mathrm{C} \qquad \textbf{Eq. 17}$$

The in-plane tortuosity of materials produced in this work was evaluated by the same radial diffusion experiment outlined in the previous section. Because the D_{eff}

produced by the experiment is interpreted as $\frac{1}{\tau}D_b$, tortuosity is measured independently of porosity[51], and can be solved for so long as the bulk and effective diffusivities are known, shown in Eq. 18.

$$\tau = \frac{D_b}{D_{eff}} \qquad \textbf{Eq. 18}$$

3.3.5 Porosity

Porosities of the electrospun and electrosprayed materials produced in this work were determined using Archimedes' principle. The principle states that, when submerged in a fluid, the buoyant force acting on an object is equal to the weight of the fluid displaced by the object, expressed in Eq. 19. The density of the fluid that the object is submerged in is ρ_l, g is the gravitational constant, and V_s is the solid volume of the material.

$$F_b = -\rho_l g V_s \qquad \textbf{Eq. 19}$$

For a fully submerged object, the total force acting on the object is the sum of the buoyant and gravitational forces, expressions for the total force and gravitational force are given in Eq. 21 and Eq. 22, where m_{sub} is the submerged mass of the object and m_{dry} is the object's mass in air.

$$F_{tot} = F_g + F_b \qquad \textbf{Eq. 20}$$

$$F_{tot} = m_{sub} g \qquad \textbf{Eq. 21}$$

$$F_g = m_{dry} g \qquad \textbf{Eq. 22}$$

Substituting Eq. 19, Eq. 21 and Eq. 22 into Eq. 20 and simplifying gives Eq. 23. Using the expression for the volume of the solid given in Eq. 24 produces Eq. 25, the central equation in this technique, allowing one to calculate the density of an object's solid material from the dry and submerged mass, assuming that the density of the fluid which the material is submerged in is known.

$$\frac{m_{dry} - m_{sub}}{\rho_l} = V_s \qquad \textbf{Eq. 23}$$

$$V_s = \frac{m_{dry}}{\rho_s} \qquad \textbf{Eq. 24}$$

$$\rho_s = \frac{\rho_l m_{dry}}{m_{dry} - m_{sub}} \qquad \textbf{Eq. 25}$$

The solid volume can be well approximated from the dry mass and the solid density, as shown in Eq. 26. This is also a good point at which to note that the

buoyancy force of displaced air is neglected.

$$V_s = \frac{m_{dry}}{\rho_s} \qquad \textbf{Eq. 26}$$

$$\varepsilon_s = 1 - \frac{V_s}{V_b} \qquad \textbf{Eq. 27}$$

Porosity of the material may then be calculated using Eq. 27. Finding the bulk volume of the object, V_b, is a question of geometry and dimensions of the object used in the experiment.

3.3.6 In-plane electrical conductivity

The in plane electrical conductivity of the backing materials used in this work was evaluated by passing current through the edge of a 1 inch square sample of the material and measuring the voltage drop across the opposite edge.

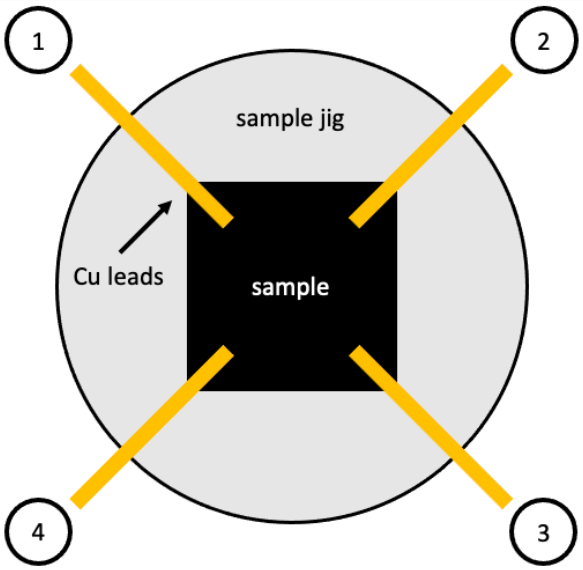

Figure 12 An illustration of the apparatus used to evaluate in-plane conductivity of backing layer materials in this work

This measurement was made across all four edges using a four probe sample holder illustrated in Figure 12 An illustration of the apparatus used to evaluate in-plane conductivity of backing layer materials in this work[56]. From the voltage drop and current data, resistance was calculated in the x and y directions, as shown in Eq. 28 and Eq. 29.

$$R_x = \frac{V_{12}}{I_{34}} \qquad \textbf{Eq. 28}$$

$$R_y = \frac{V_{23}}{I_{14}} \qquad \textbf{Eq. 29}$$

The electrode materials studied may be approximated as two dimensional materials, the x and y dimensions being orders of magnitude greater than the z

dimension (thickness), allowing the van der Pauw method to be used to solve for the in-plane resistance of the sheet, R_s, using Eq. 30[57].

$$e^{-\frac{\pi R_x}{R_S}} + e^{-\frac{\pi R_y}{R_S}} = 1 \qquad \textbf{Eq. 30}$$

Electrical conductivity of the sample, σ_s, was then solved for, knowing the in-plane resistance, R_s, and sample thickness, t, using Eq. 31.

$$\sigma_s = \frac{1}{R_s t} \qquad \textbf{Eq. 31}$$

Bolts on the sample jig were each tightened to 2 Nm in order to reduce contact resistance between the electrodes and the copper leads. 2 Nm of torque was shown to slightly decrease sheet resistance across a range of electrode materials, while higher torque values increased sheet resistance in fibrous electrodes, likely due to damaged fibers[56].

3.4 Test cell design and electrochemical characterization

A simple test cell was designed using as many off the shelf parts as possible. Two threaded male and female ABS socket connectors comprised the outer casing of the test cell and compressed the internal components of the cell as they were screwed together. The internal components of the cell were assembled in the female ABS component from the bottom to up (cathode side to anode side), as illustrated in Figure 13.

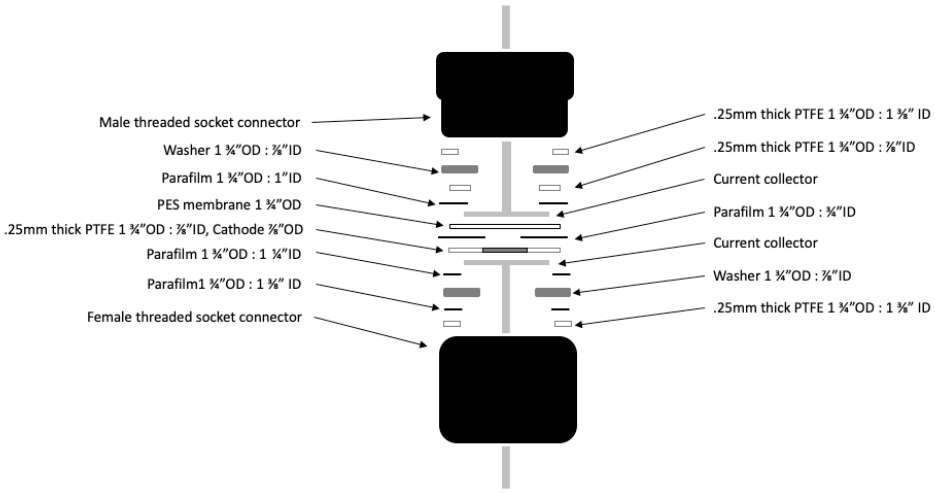

Figure 13 A schematic of the test cell designed for electrochemical characterization

Teflon gaskets were used to both arrange cell components and provide a watertight seal. A Sterlitech PES membrane with .45 micron pores was used as a separator, allowing electrolyte to reach the catalyst layer on the cathode while providing electrical separation between the anode and cathode. As preliminary cell designs were being tested it became clear that Teflon gaskets were not adequate to prevent electrolyte leakage and Parafilm gaskets were added at critical points to address the problem.

On the anode side of the cell the same nickel mesh used as a backing layer in the Zinc8 material served as a current collector with a tab of the mesh extending from the cell allowing for the connection of electrical probes. The cathode current collector was also nickel mesh, making contact with the air side of the gas diffusion layer.

Leads from a Bio-Logic SAS potentiostat, model SP-150, were connected to the tabs on the anode and cathode current collectors. EC Lab software was used to control the potentiostat and record current and voltage values. Polarization curves were

measured by varying the voltage from the open cell voltage to 1.2 V below the open cell voltage.

A 30 cm long cylindrical chamber was added to the bottom (cathode side) of the test cell, with a flow line ported in, so that oxygen concentration at the air cathode could be controlled. A mixture of air and nitrogen was fed into the chamber, each gas controlled by a separate flow controller. The lead for the cathode side current collector was fed through a hole in the chamber, space around the lead and hole was filled with putty. Gases were fed at a total volumetric flow rate of .5 standard liters per minute (SLM). Polarization curve measurements were taken 15 minutes after gas concentration changed to allow for complete displacement of the previous gas mixture.

3.5 Reference material overview

The reference cathode material currently being used in zinc air cells is a gas diffusion layer composed of carbon powder and 50wt% PTFE binder pressed into an expanded nickel mesh current collector that also serves to provide structural integrity. A catalyst layer of platinum on carbon with 25wt% PTFE is applied on the side opposite the nickel mesh, with a loading of .4 $mgPt/cm^2$.

Figure 14 shows the nickel mesh integrated with the carbon powder GDL as well as the microstructure of the catalyst layer. The small pore size in the powder/binder matrix, and the high PTFE loading results in a high breakthrough pressure of 874 kPa.

Electrosprayed catalyst layers with a platinum loading of $.4mg/cm^2$ were also applied to the reference backing material to directly compare the performance of the

GDLs studied in this work. The electrodes made from the reference backing layer with Nafion and PTFE catalyst layers were named R_N and R_P respectively.

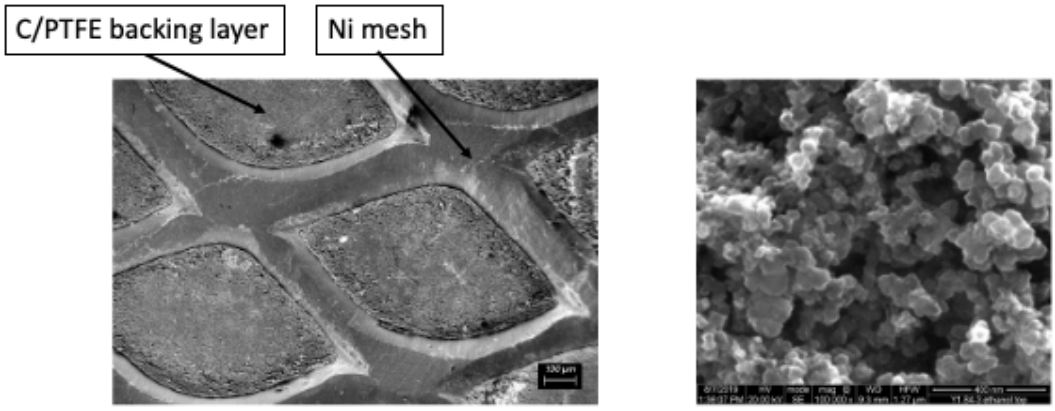

Figure 14 SEM images of the Ni mesh/backing layer integration (left) and the microstructure of the catalyst layer (right)

4 Results

4.1 Design considerations for electrospun fibers

The bulk of commercially available gas diffusion layers are made from a carbon cloth loaded with PTFE and are designed for PEMFC applications. For zinc – air cells a carbon powder/binder material with an average pore size below 100nm is currently being used. The gas diffusion layer in a zinc air battery serves many purposes such as mechanically supporting the catalyst layer and acting as a conductor for electrons participating in ORR and OER reactions. But, the most important functions of the GDL are mass transport related; an ideal GDL allows oxygen to diffuse to the catalyst layer with little resistance while preventing electrolyte from invading the pores and flooding the cell.

In an effort to optimize for both gas diffusion and water management, electrospinning parameters were selected to achieve the smallest fiber diameter possible, in turn reducing the pore size of the material. The Washburn equation, Eq. 32, demonstrates that the capillary pressure required for water to invade pores has an inverse relationship to pore size, and higher capillary pressures required to force water into the pores, aka breakthrough pressures, are desirable to prevent cell flooding.

$$P_c = \frac{-2\,\sigma\cos\theta}{r} \qquad \textbf{Eq. 32}$$

It is therefore advantageous to reduce the pore sizes, if possible. However,

effective diffusivity also decreases when the pore sizes are below 1 um due to Knudsen effects [58]. Ultimately, though reducing fiber diameter reduces the pore sizes in the fiber matrix, the pores are still much larger than the diffusing species (oxygen molecules) and Knudsen diffusion is insignificant.

4.2 Design considerations for an electrosprayed microporous layer

The microporous layer serves to block electrolyte in the catalyst layer from further invading the cathode. As such, a high degree of hydrophobicity is desirable and can be achieved by engineering the pore size and material composition of the MPL. Because reactants and products must diffuse across the MPL it is desirable to minimize the layer thickness. Carbon and PTFE content in the MPL was defined to mimic the composition of the commercial backing layer material. The thickness of the electrosprayed MPL was controlled by the flow rate and number of passes made during its application and the thinnest uniform layer was targeted.

4.3 Design considerations for an electrosprayed catalyst layer

Catalyst loading, expressed in mg/cm^2, is one of the most critical parameters for the catalyst layer from both a cost and performance perspective. .4 $mgPt/cm^2$ is a common catalyst loading, and was the loading targeted in developing the GDE material. A PTFE concentration of 25wt% was used in the catalyst layer, the same as the commercial material. The lower PTFE loading was used to allow for more electrolyte invasion into the catalyst layer, making more catalytic sites accessible. The use of less hydrophobic binder materials can also promote electrolyte invasion in the catalyst layer, and catalyst layers with a Nafion concentration of 30wt% were

evaluated in this work.

4.4 Electrospun fiber production and characterization

Free standing mats of electrospun carbon fibers were developed as gas diffusion layer materials. Fabrication of the final PTFE loaded fiber product is a three-step process. Characterization work was performed for both the intermediate and final products and is presented for each step in the following subsections.

Experiments were conducted to determine the lowest concentration PAN/DMF that was electrospinnable and would produce fibers with a consistent cylindrical shape. Solutions below 8wt% produced beaded fibers, and the lower viscosity of 8wt% solutions made electrospinning at reasonable flowrates without the PAN/DMF solution dripping from the needle impractical. 9wt% PAN/DMF solutions were found to be the lowest concentration that produced uniform fibers that was readily electrospinnable on the apparatus used in this work.

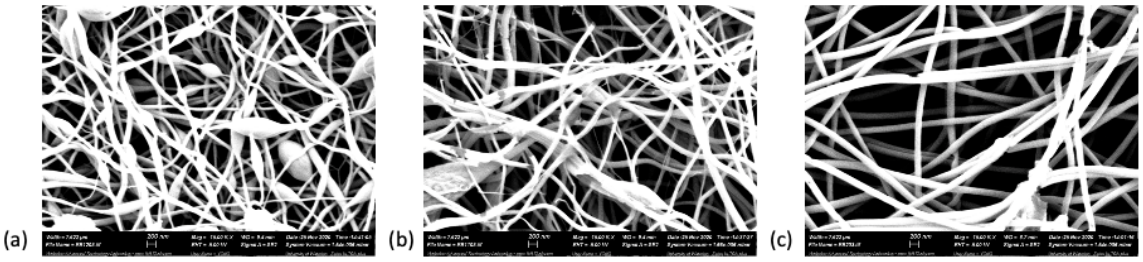

Figure 15 SEM images illustrating the change in fiber morphology with polymer concentration in solution, (a) 6wt%, (b) 7wt%, (c) 9wt%

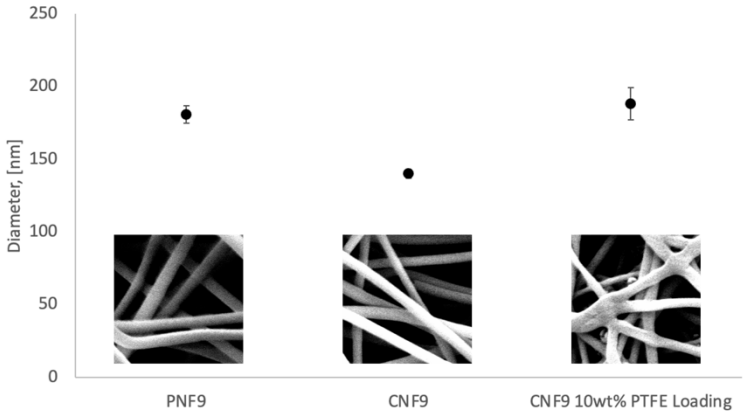

Figure 16 Fiber diameters for each step in the electrospun GDL production process. The inset images are 2x2 mircon areas of the fiber mats.

Figure 16 displays the average fiber diameter at each step in the development of the electrospun GDL materials. First, PAN fibers are electrospun, PAN9 are fibers produced from a 9wt% PAN/DMF solution. Then the PAN is carbonized, and fiber size reduces, producing a mat of carbon nanofibers (eg CNF9). Finally, the carbon fiber mat is treated with DISP 30, a PTFE dispersion, and the PTFE is sintered, coating the fibers and accumulating at fiber junctions.

4.4.1 SEM images and fiber properties

PAN fibers produced from a 9 wt% PAN/DMF solution feature a consistent cylindrical morphology and have an average diameter of 180 nm. During carbonization the morphology is preserved, and average fiber diameter decreases to 140 nm.

Table 4 Mean fiber diameters for PAN and CNF produced from a 9wt% PAN/DMF solution

	Mean fiber diameter ± std. error, [nm]
PAN9	181 ± 6
CNF9	140. ± 3

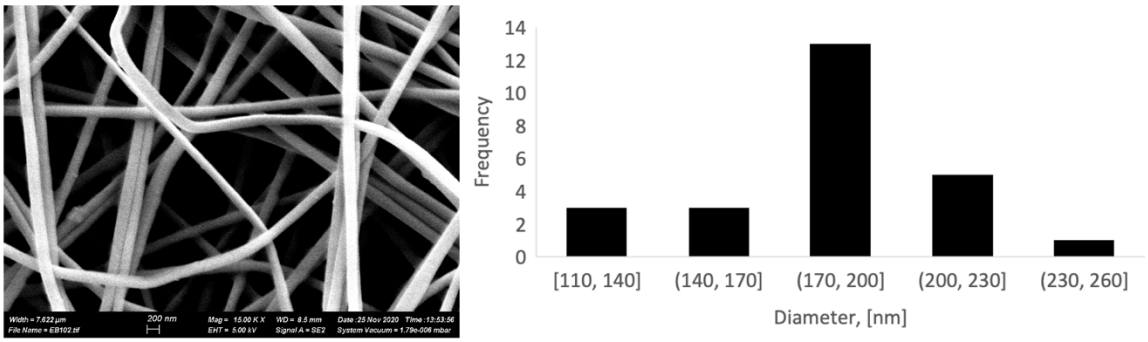

Figure 17 SEM image of PAN fibers electrospun from a 9wt% PAN/DMF solution (left) and a histogram of fiber sizes (right)

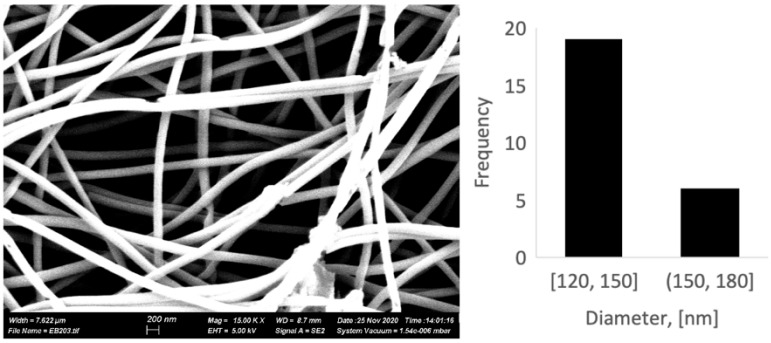

Figure 18 SEM image of carbon fibers from an electrospun 9wt% PAN/DMF solution (left) and a histogram of fiber sizes (right)

4.4.2 Teflon loading

The technique to achieve a desired weight percentage of Teflon is outlined in Section 3.2.4 Teflon coating. SEM images of Teflon coated carbon fibers are presented in Figure 19, with the Teflon particularly visible at the fiber intersections. Characterization work was performed to understand the degree to which Teflon coating the fibers effected properties of the system. The porosity and effective diffusivity were only slightly reduced while breakthrough pressure significantly increased.

Table 5 Mean fiber diameter CNF produced from 9wt% PAN/DMF and 10 wt% PTFE loading

	Mean fiber diameter ± std. error, [nm]
CNF9, 10wt% PTFE	188 ± 11

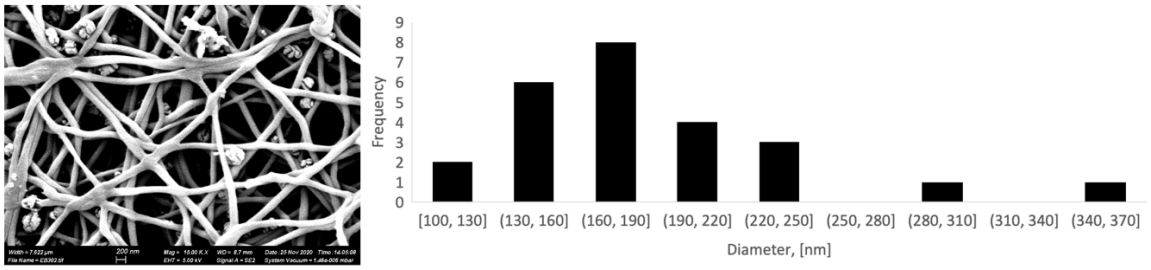

Figure 19 SEM image of carbon fibers electrospun from a 9wt% PAN/DMF solution coated with 10wt% PTFE(left) and a histogram of fiber sizes (right)

4.5 Porosity

Table 6 Porosity of raw PAN and carbon fiber mats

	Mat thickness, [μm]	Porosity
PAN9	418	67.3%
CNF9	143	88.6%
CNF9_P	N/A	87.6%
MPL	53	86.1%
CL	28	81.1%
SGL 25 BC*	235	76%
R*	481	75%

* Reported by manufacturer

Porosity of the materials developed in this work was evaluated with Archimedes' principle, described in Section 3.3.5.

Mass loss during the carbonization process is reflected in the change in porosity of the fiber materials. Raw PAN mats are thicker and have less void space (more solid volume) than the mats of carbon fibers. Fiber diameter decreases by roughly 22% when PAN9 is carbonized. Assuming cylindrical fibers and neglecting any reduction in fiber length, this reduction in diameter should correspond to a 40%

decrease in solid volume.

The actual porosity of the fiber materials increased by 32%, not 40%, following carbonization. This discrepancy can be accounted for by considering the change in mat thickness before and after carbonization. The mat thickness should change in proportion to the fiber diameter, if it is assumed that the mat is composed of fibers layered on top of each other in direct contact. Mat thickness, however, was found to decrease by 66%. From this result it can be concluded that the carbonization technique compressed the fiber mat to some degree. Extending further, the PAN fibers can be visualized as having more variation in their z position, undulating up and down, making less contact with their neighbours in layers below and above. Sandwiching the PAN sheets between carbon plates before loading them into the tube furnace reduces this undulation.

The reduction in porosity as a result of Teflon loading can be calculated from the difference in pre and post PTFE loading mass knowing the density of PTFE (2.2 g/m^3). For the CNF9 material 10 wt% PTFE loading was targeted and 10.3wt% loading was achieved, corresponding to a 1.2% decrease in porosity, from 88.6% to 87.6% void space.

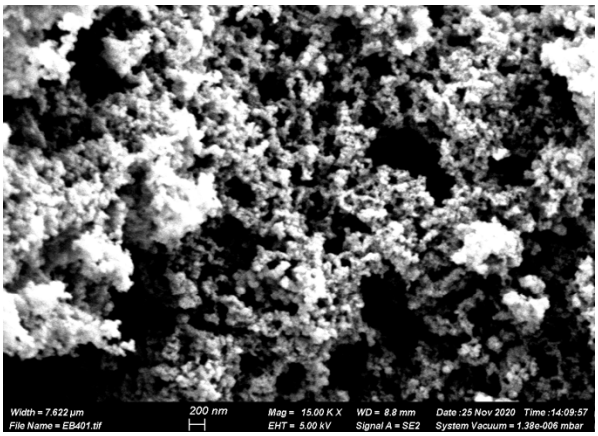

Figure 20 A SEM image of the electrosprayed microporous layer, illustrating the amorphous morphology of the MPL

Microporous layers of at least 50 microns were electrosprayed onto copper foil to measure the porosity and effective diffusivity. The porosity of these electrosprayed MPLs was found to be 86.1%, while catalyst layers were electrosprayed onto copper foil were found to have a porosity of 81.8%.

4.6 Effective diffusivity and tortuosity

The effective diffusion coefficient, D_{eff}, and tortuosity, for raw PAN fibers and carbon fibers is presented in Table 7. The reduction in solid volume that occurs during carbonization increases the effective diffusion coefficient and reduces the amount of tortuosity in the pore space of the fiber mat.

Table 7 Effective diffusion coefficient and tortuosity for electrospun PAN and carbon fibers

	$D_{eff,}$ [cm^2/s] ± std. error	τ ± std. error
PAN9	0.159 ± .012	1.26 ± .09
CNF9	0.171 ± .019	1.17 ± .13
CNF9, 10wt% PTFE	0.165 ± .006	1.21 ± .04
MPL, 50wt% PTFE	0.148 ± .016	1.35 ± .15
Reference Backing Layer	.096 ± .003	2.09 ± .05

10 wt% PTFE loading on the fibers was shown to decrease the effective diffusion coefficient and increase tortuosity of the fiber mat by roughly 3% compared to untreated carbon fibers. The microporous layer is the final material that oxygen diffuses though before reaching that catalyst, meaning that the diffusivity of oxygen though the amorphous isotropic MPL is an important characteristic of the GDE. The electrosprayed MPL was designed to have the same composition as the reference material, a carbon powder which provides the pore structure and PTFE loading of 50wt%, acting as a binder. Though Teflon loading in the MPL and reference backing layer was similar, the electrosprayed MPL was shown to have an effective diffusion coefficient ~1.5 times higher than that of the reference backing layer.

4.7 Breakthrough pressure

Breakthrough pressure experiments were performed to determine the optimal PTFE loading. 10 wt% PTFE loading was determined to be optimal, resulting in a breakthrough pressure of 147 kPa.

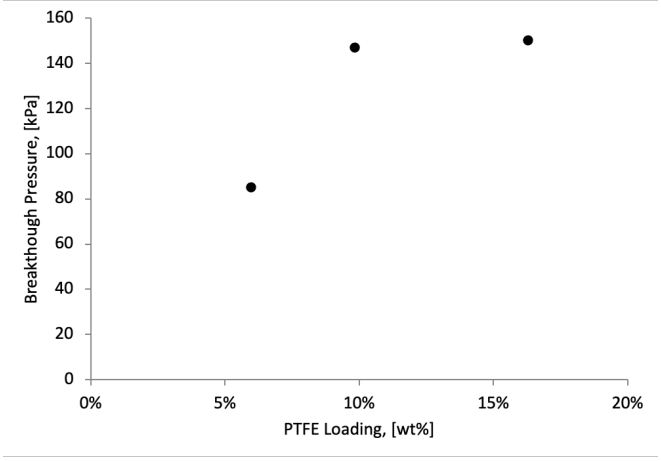

Figure 21 Breakthrough pressure as a function of PTFE loading

Table 8 Breakthrough pressure of backing layer materials produced in this work

	Breakthrough Pressure [kPa]
CNF9 10wt% PTFE	147 kPa
CNF9 10wt% PTFE + MPL	192 kPa
R	847 kPa

Experiments were performed with electrospun material that had an electrosprayed MPL on one side, breakthrough pressure was found to be 192 kPa, 45 kPa higher than electrospun fibers with 10wt% PTFE loading alone. Compared to the breakthrough pressure of the reference backing material, PTFE loaded electrospun fibers with an electrosprayed MPL is significantly lower. This may be attributed to the larger pore size and higher porosity of the electrospun/electrosprayed materials produced in this work.

4.8 BET specific surface area

Table 9 BET specific surface area of PTFE coated fibers

	S_{BET}, [m^2/g]	Relative Pressure Range
CNF9 with 10wt% PTFE	9.81	30 – 70%
CNF9 with 10wt% PTFE + MPL	10.07	22.5 – 45%
CNF9 with 10wt% PTFE + MPL + CL	39.6	17.5 – 27.5%
CL	146	n/a

The specific surface area of PTFE coated fibers was found to be 9.81 m^2/g, calculated from cyclohexane adsorption at 25 °C. Valid specific surface area values for the system ranged from 2.81 to 9.81 m^2/g, the relative pressure interval that best fit BET theory produced a specific surface area answer of 9.59 m^2/g.

The specific surface area of PTFE coated fibers with an electrosprayed MPL was found to be 10.07 m^2/g, calculated from cyclohexane adsorption at 25 °C, the increase

is due to the application of the MPL with a higher specific surface area than the electrospun fibers. Valid specific surface area values for the system ranged from 5.23 to 10.1 m^2/g. Note that, for the materials with high porosity layers electrosprayed applied there are no valid relative pressure ranges above 45%; at higher relative pressures as pores fill steric limitations and interactions with surrounding adsorbed molecules cause the isotherm to deviate from BET theory.

The specific surface area of PTFE coated fibers with an electrosprayed MPL was found to be 39.6 m^2/g, calculated from cyclohexane adsorption at 25 °C, much higher than carbon fiber mats due to the contribution of surface area in the catalyst layer. Figure 36 is a heatmap of valid specific surface answers for the adsorption system and may be found in the Appendix. Valid specific surface area values for the system ranged from 28.6 to 39.6 m^2/g.

4.9 Conductivity

Conductivity of backing layer materials developed in this work was evaluated using the van der Pauw technique described in Section 3.3.6 and is presented in Table 10.

Table 10 In-plane electrical conductivity for the materials developed in this work

	σ_s, [S/m]
R	101
R + Ni	6.71×10^5
CNF9	464
CNF9 with 10wt% PTFE	92.1
SGL 25 BC	3.01×10^3

The reduction in conductivity after Teflon loading the electrospun fibers may be attributed to PTFE accumulating at the fiber junctions, reducing contact between the fibers, reducing the in-plane conductivity of the material. Lower conductivity cathode materials increase the internal resistance of the cell, resulting in higher ohmic losses observed during polarization curve experiments. Integrating a metal mesh current collector into the porous gas diffusion material, as was done for the R + Ni material, both increases the conductivity of the electrode while providing mechanical support.

4.10 Electrochemical performance

The electrochemical performance of seven different cathode designs were investigated by combining different substrates with different catalyst layers. The matrix of tested materials and the naming scheme are organized in Table 11. These experiments were designed to evaluate the performance of electrospun and electrosprayed GDEs and compare them to commercial materials used in zinc air batteries and PEM fuel cells. Nafion and PTFE were compared as catalyst layer binder materials to determine if increased electrolyte invasion in the catalyst layer when Nafion is used improved electrochemical performance of the cathode.

Table 11 Matrix of cathode material designs explored in this work, summarizing relevant properties

Gas Diffusion Layer \ Catalyst Layer	Reference	Electrosprayed with PTFE	Electrosprayed with Nafion
Reference	R ε: 75% D_{eff}: .096 cm^2/s τ: 2.09 Thickness: .5mm .4mg Pt/cm^2, 25wt% PTFE	R_P ε: 75% D_{eff}: .096 cm^2/s τ: 2.09 Thickness: .5mm .4mg Pt/cm^2, 25wt% PTFE	R_N ε: 75% D_{eff}: .096 cm^2/s τ: 2.09 Thickness: .5mm .4mg Pt/cm^2, 30wt% Nafion
Electrospun GDL		CNF9_P ε: 87% D_{eff}: .165 cm^2/s τ: 1.21 Thickness: .261mm .4mg Pt/cm^2, 25wt% PTFE	CNF9_N ε: 87% D_{eff}: .165 cm^2/s τ: 1.21 Thickness: .261mm .4mg Pt/cm^2, 30wt% Nafion
SGL 24 BC		SGL_P ε: 75% D_{eff}: .133 cm^2/s τ: 1.45 Thickness: .270mm .4mg Pt/cm^2, 25wt% PTFE	SGL_N ε: 75% D_{eff}: .133 cm^2/s τ: 1.45 Thickness: .270mm .4mg Pt/cm^2, 30wt% Nafion

4.10.1 SGL_P and SGL_N material overview

PTFE and Nafion catalyst layers were applied to Sigracet GDL 25 BC (abbreviated SGL) gas diffusion layers to compare the performance of the electrospun GDL produced in this work to commercially available GDL materials. SGL24BC has an advertised porosity of 76% and a total thickness of 235 μm. The fibers are loaded with 5wt% PTFE, and a 45 μm thick microporous layer applied to one side of the fibers. Figure 22 shows the PTFE loaded fibers and microporous layer morphology, with PTFE clearly bridging between fibers. The average fiber and pore size of SGL24BC

were measured from the images and found to be 9 μm and 100 μm, both larger than the electrosprayed GDL.

Catalyst layers with a Pt loading of .4mg/cm^2 were applied with the same electrospraying techniques used thought out this work. Both Nafion and PTFE were used as binder materials, and the electrodes produced were named SGL_N and SGL_P respectively.

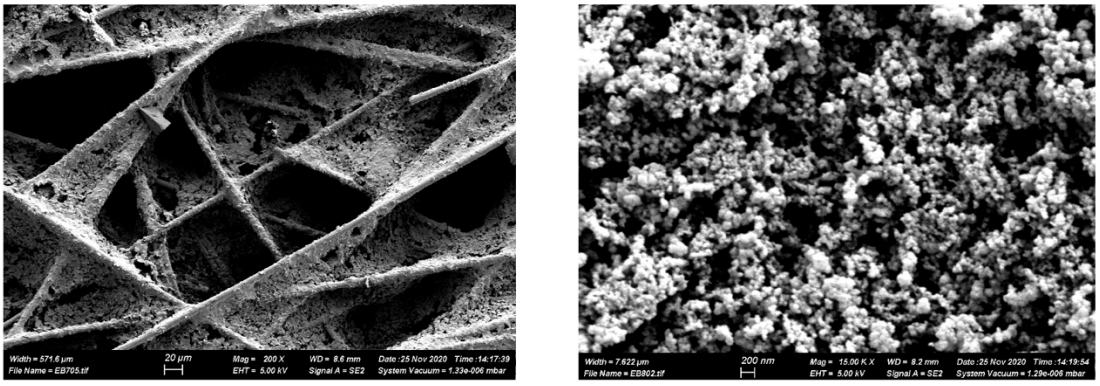

Figure 22 SEM images of the fiber structure (left) and microporous layer (right) of and SGL BC 24 gas diffusion layer

4.10.2 Electrospun and electrosprayed GDE overview

Sheets of electrospun carbon fibers were produced from a 9wt% PAN/DMF and loaded with 10wt% PTFE in this work. An MPL was electrosprayed onto one side of the fiber sheet to increase breakthrough pressure, acting as a barrier to electrolyte invading the GDL.

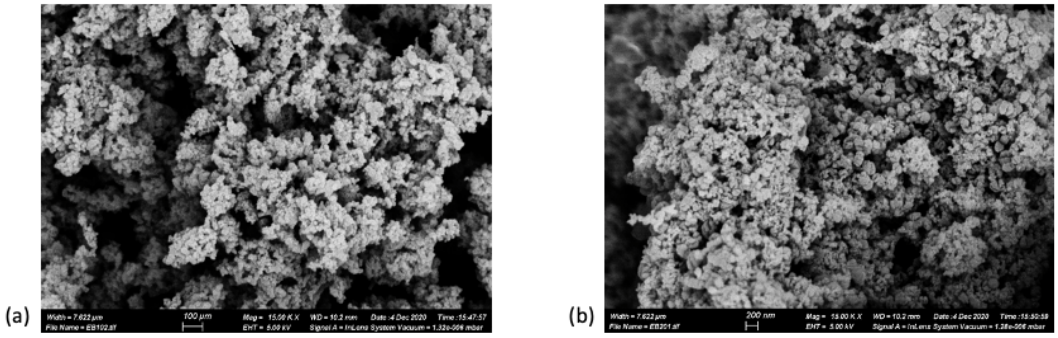

Figure 23 SEM images of electrosprayed catalyst layers using (a) PTFE and (b) Nafion, as binder materials

Nafion and PTFE catalyst layers with a platinum loading of .4mg/cm^2 were electrosprayed onto the MPL, producing materials with an average total thickness of .261mm. The electrospun carbon nanofiber electrodes with Nafion and PTFE catalyst layers were named CNF9_N and CNF9_P respectively.

4.10.3 Polarization curves

Polarization curves were measured for all cathode materials developed in this work, as well as for the reference electrode material. The nickel mesh was removed from the reference electrode as the other materials did not have an integrated current collector.

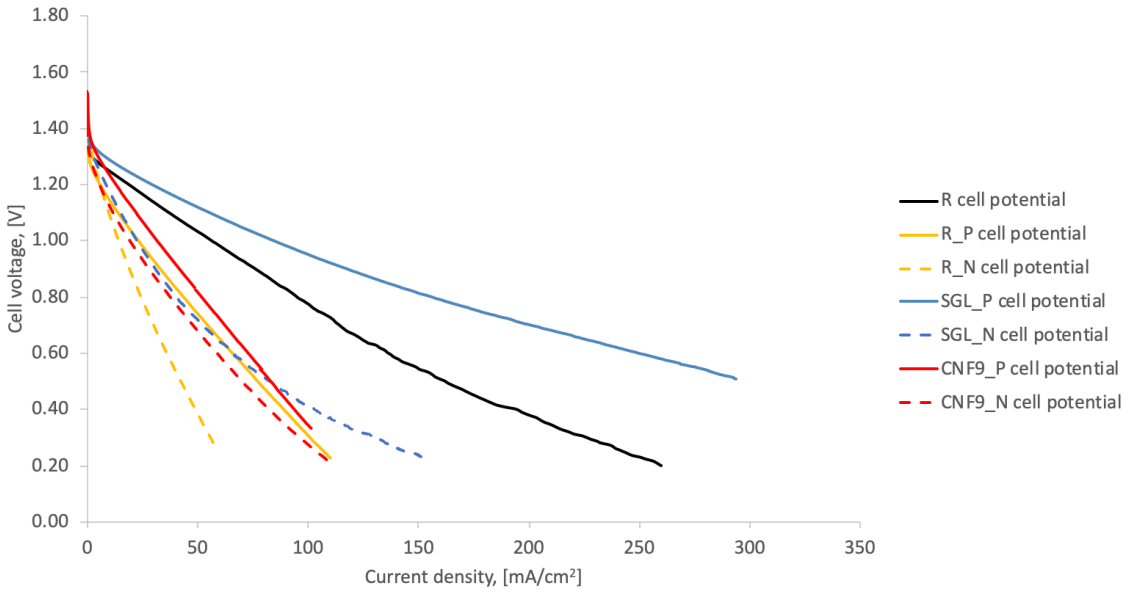

Figure 24 Polarization curves for a variety of cathode materials

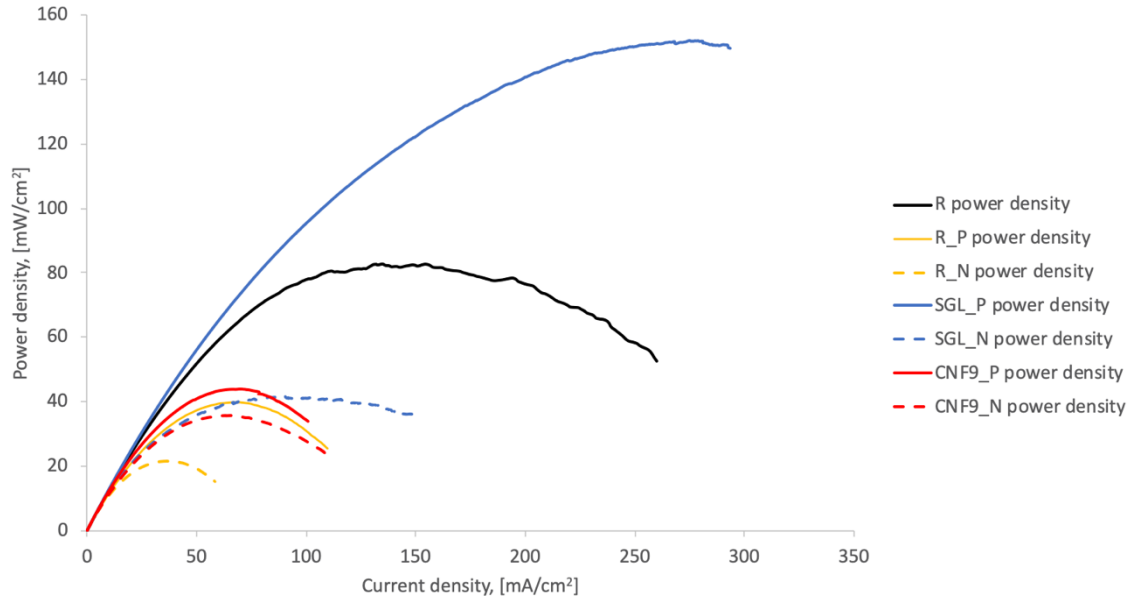

Figure 25 Power density as a function of voltage for various cathode materials

The polarization curve experiments showed that the SGL gas diffusion layer with a PTFE loaded catalyst layer performed significantly better than the reference

commercial material. An encouraging result, suggesting that the morphology of electrosprayed catalyst layers is an improvement over conventional design. Catalyst layers with 25wt% PTFE loading outperformed electrodes with 30wt% Nafion loading for all the material designs studied. This may be due to more electrochemically active surface area available in the PTFE catalyst layer. Differences in the behavior of electrolyte invading the PTFE and Nafion catalyst layers may also explain the poorer electrochemical performance of the Nafion catalyst layers. Additionally, when oxygen is reduced at the cathode hydroxide ions are created and Nafion binder in the catalyst layer could limit their mobility away from the triple phase boundary enough that electrochemical performance is reduced.

The poor performance of the electrospun materials was unexpected, as the electrospun fiber materials have significantly more favorable mass transport properties. There are several hypothesizes as to why the electrospun materials performed poorly. PTFE coating of the fibers that reduces sheet conductivity increases ohmic losses, and PTFE loading/sintering may inhibit mass transport. Characterization work showed that radial diffusion in electrospun materials was not significantly impacted by PTFE loading, however through plane diffusivity may be reduced by PTFE in the electrospun cathodes. Migration of PTFE to the surface of electrospun fibers would reduce through plane diffusion and increase contact resistance with the current collector, and unfavorable morphology at the interface of 50wt% PTFE MPL and the 10wt% PTFE GDL could also limit through plane diffusivity.

4.10.4 PTFE coating of electrospun carbon fibers

In an attempt to determine the root cause of poor electrospun material performance, experiments were conducted with an electrospun fibrous mat placed under an SGL_P cathode (in between the cathode and the current collector), shown in Figure 27. Polarization curve measurements were taken for the combined SGL electrode and bare carbon fibers (SGL_P + CNF9) as well as for the SGL electrode with PTFE coated carbon fibers (SGL_P + CNF9_P).

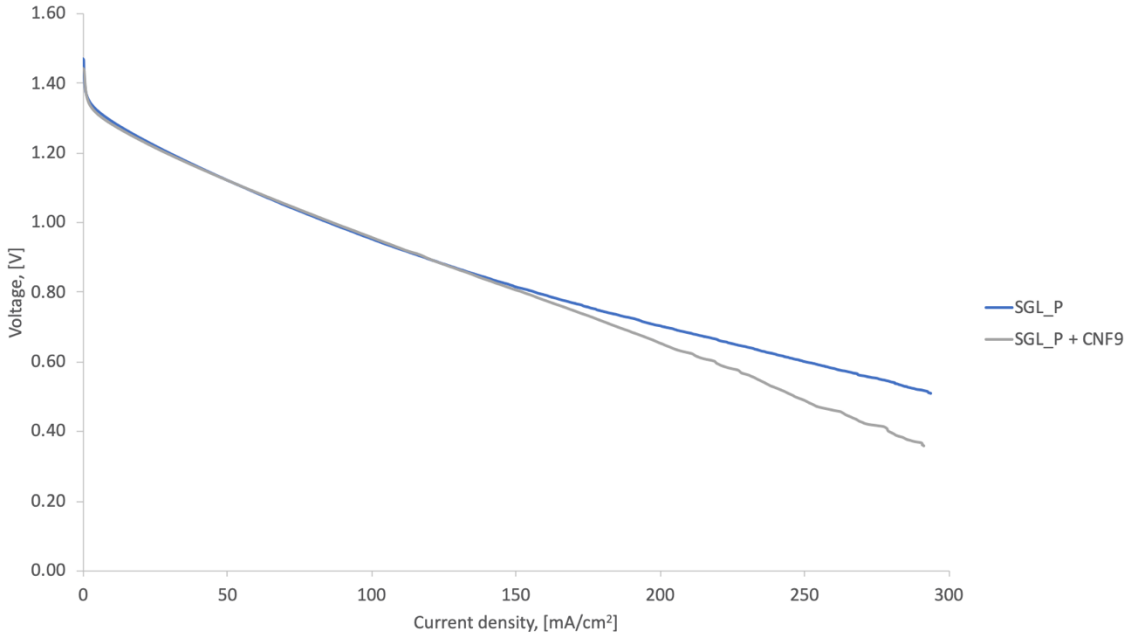

Figure 26 Polarization curves comparing SGL_P and SGL_P + CNF9 cathodes

The combined SGL_P+CNF9 material exhibited similar ohmic losses, and mass transfer limitations at current densities above 150 mA/cm^2, suggesting that the conductivity of the electrospun carbon fibers is high enough that they do not appreciably contribute to the internal resistance of the zinc air cell and that the contact between the electrospun fibers and the current collector is comparable to

current collector contact with SGL electrodes. The mass transfer limitations may be attributed to the fact that electrode thickness is doubled for the SGL_P + CNF9 material, doubling the amount of porous gas diffusion media that oxygen must diffuse though before reaching the triple phase boundary.

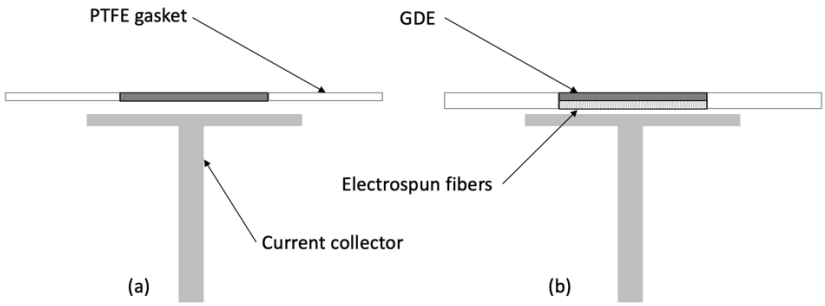

Figure 27 (a) standard electrode arrangement in the test cell, (b) arrangement of the electrode with electrospun fibers inserted below the GDE

A similar experiment, with a sheet of electrospun fibers coated with 10wt% PTFE inserted underneath an SGL_P was performed. Electrode performance was significantly reduced, shown in Figure 28, much more so than in the experiment with uncoated electrospun fibers. This suggests that loading the fibers with PTFE can increase the contact resistance enough to impact the cathode performance, supporting the hypothesis that the poor performance of the electrospun cathodes, shown in Figure 24 and Figure 25 Power density as a function of voltage for various cathode materials, is due to the contact resistance between PTFE coated fibers and the test cell current collector.

Note that this effect may be exaggerated due to the construction of the test cell used to produce these polarization curves. Inconsistent compression of cell components, for example, can cause variation in contact resistance between the GDL

and current collector. However, the result is still useful in illustrating that the design of electrospun cathodes must consider current collector integration with the electrospun GDL. Effective GDL and current collector design should both increase conductivity of the cathode side of the cell, but also increase the structural integrity of the cathode.

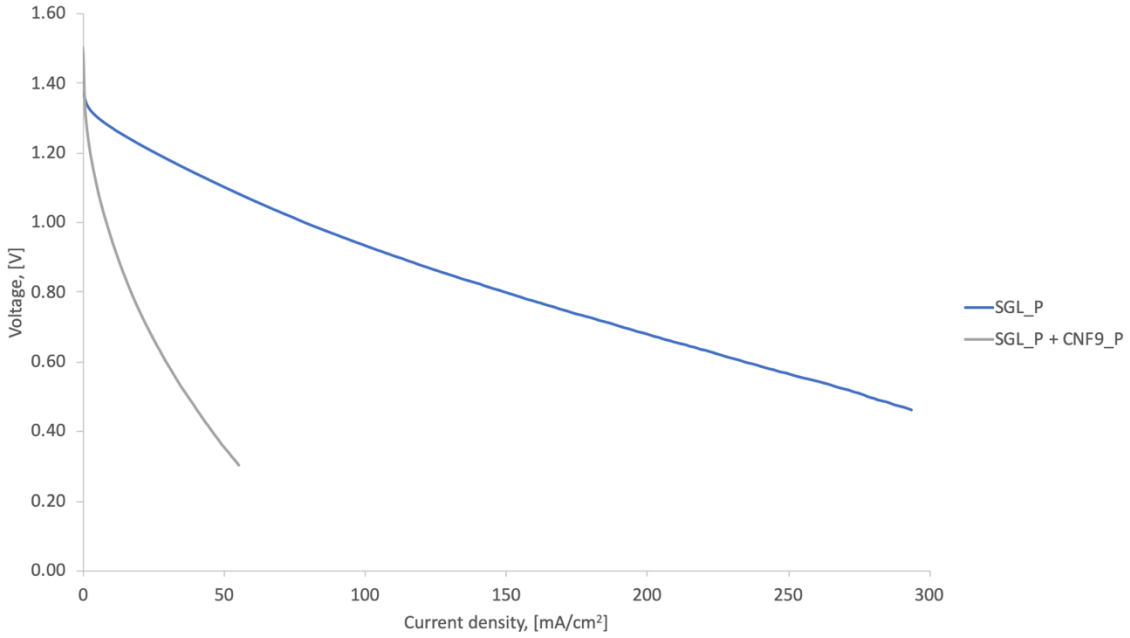

Figure 28 Polarization curves comparing SGL_P and SGL_P + CNF9_P cathodes

The results of experiments combining SGL_P and electrospin fibers led to the development of an electrospin electrode with bare carbon fibers (i.e. no PTFE loading on the fibrous gas diffusion layer). Polarization curves for this bare carbon fiber electrode (CNF9_P bare fiber) are presented in Figure 29 and compared to the performance of the reference electrode and the electrospin electrode with PTFE coated carbon fibers. Performance was clearly improved in the bare carbon fiber electrode, outperforming both the commercial (R) and CNF9_P electrodes.

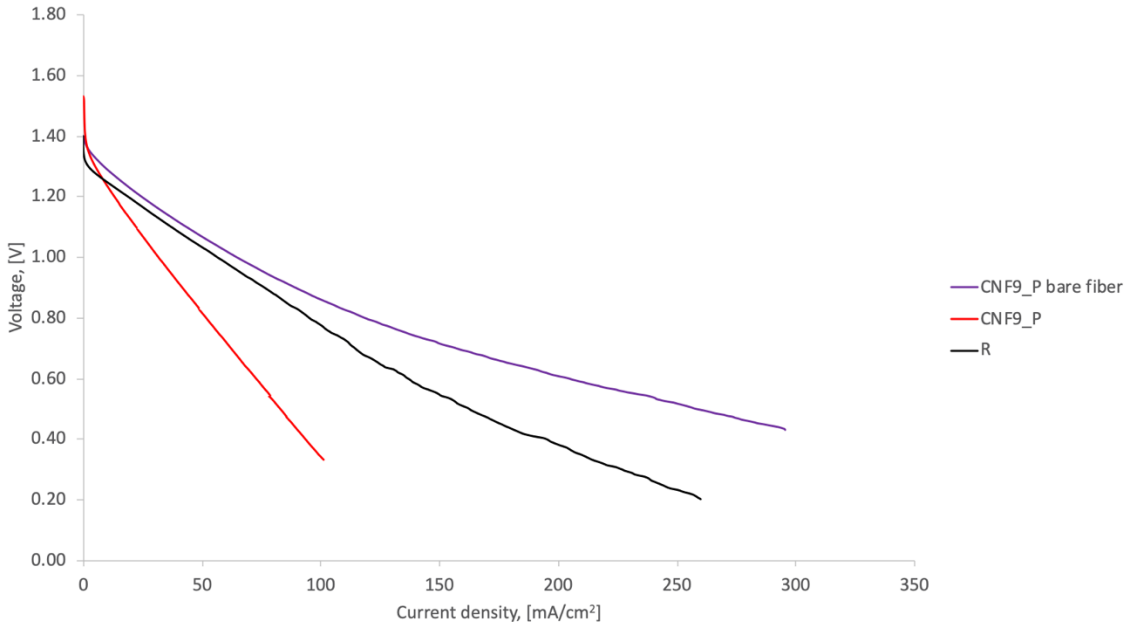

Figure 29 Polarization curves comparing the performance of CNF_P and CNF9_P with bare fibers, commercial material (R) performance included for reference

Ohmic losses for the CNF9_P bare fiber electrode are similar to the commercial electrode, while lower activation potential losses are observed. The decrease in ohmic losses between CNF9_P and the bare fiber electrode can be attributed to less contact resistance between the fibers and the current collector in the test cell and to the improved in-plane resistance of the bare carbon fiber materials compared to PTFE coated fibers. The improvement in activation potential between the R and CNF9_P bare fiber materials may be attributed to the favorable morphology of electrosprayed catalyst layers, compared to the commercial cathode materials.

Practically, the cathode design with bare carbon fibers is not realistic, as the hydrophobic characteristics of untreated carbon fibers can lead to water accumulation in the gas diffusion layer from condensation, limiting oxygen diffusion to the catalyst layer. Better integration of the current collector and carbon fibers may

reduce ohmic losses in PTFE loaded materials, and that alternative surface treatments of the fibers may be warranted.

4.10.5 PTFE loading in the CL

To confirm the relationship between PTFE loading in the catalyst layer of air cathode, polarization curve experiments for air cathodes with various CL designs were performed. In general, lower PTFE loading corresponded to improved cathode performance.

Catalyst layers with PTFE loading of 10, 15, and 25wt% were electrosprayed onto an SGL 24 BC substrate with a catalyst loading of .4mgPt/cm^2. Polarization curve experiments showed that the catalyst layer with 10% PTFE loading performed best, exhibiting lower ohmic losses and lower activation potential than the 15 and 25wt% material.

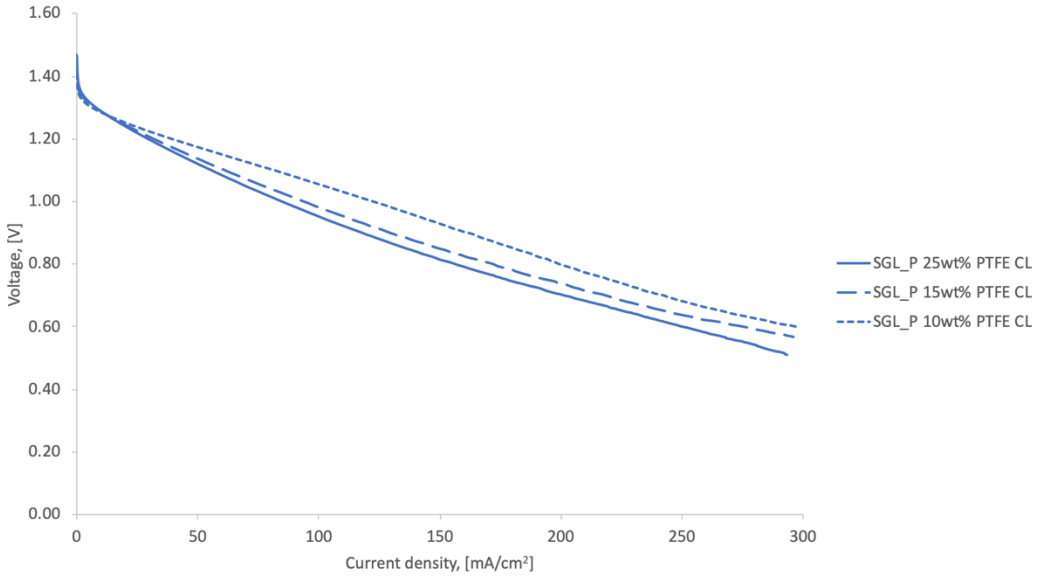

Figure 30 Polarization curves for electrodes with electrosprayed catalyst layers with varying PTFE loading

These results, as well as the experiments with PTFE coated fibers and bare carbon fibers under an SGL_P electrode, demonstrate the impact of incorporating PTFE in ZAB electrodes. Optimization work to determine the lowest possible PTFE loading the CL without significantly impacting durability will be valuable in improving air cathode performance. Additionally, alternative surface functionalization of fibers in the gas diffusion layer may be a path to improving conductivity of the GDE without compromising hydrophobic properties [59].

4.10.6 Mass transfer effects

Polarization curve experiments with varying ratios of air and nitrogen were first fed into the cathode side of the test cell with a reference electrode that still had the integrated nickel current collector. Concentration polarization was observed with an air-nitrogen ratio of .2 (3.5% oxygen) and total flow rate of .5 standard liters per minute. These effects occurred to a lesser degree after doubling the air:N_2 ratio (6% oxygen).

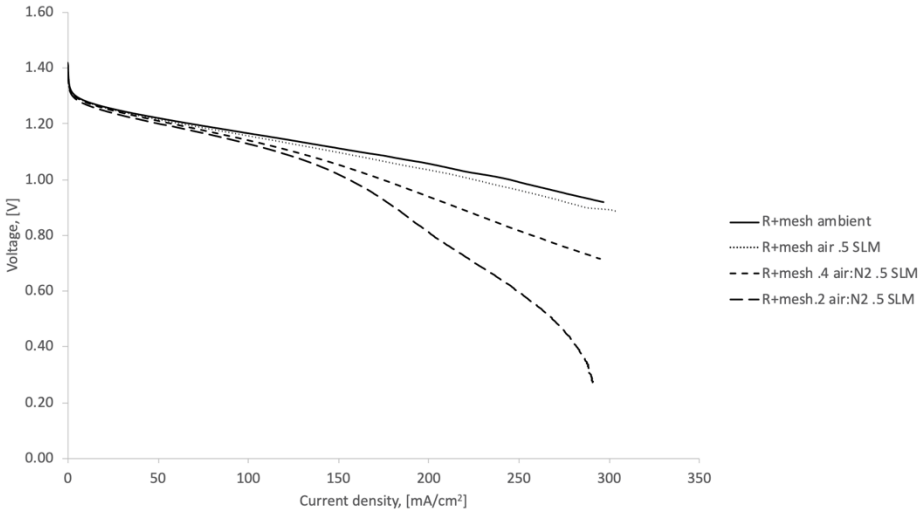

Figure 31 Limited oxygen concentration experiments for the reference material with integrated nickel current collector

Similar experiments were conducted for the SGL_P and CNF9_P bare fiber electrodes. The polarization curve experiments for the CNF9_P bare fiber material illustrate the benefits of improved mass transfer in the GDL. Mass transfer limitations were observed at high current densities for the .2 air:N_2 ratio.

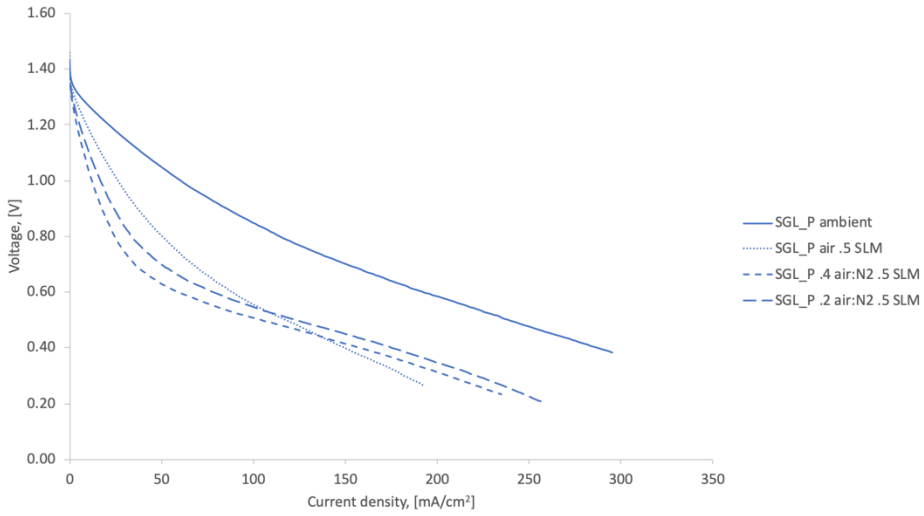

Figure 32 Limited oxygen concentration experiments for the SGL_P electrode

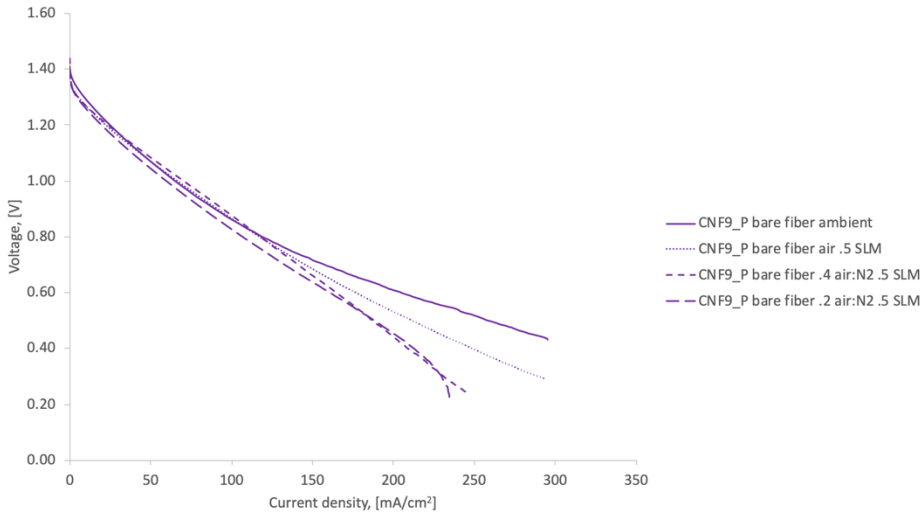

Figure 33 Limited oxygen concentration experiments for the CNF9_P electrode with bare carbon fibers

The results of these mass transfer experiments support the effective diffusivity characterization work that showed the SGL and electrospun materials offer improved mass transport compared to commercial powder-binder gas diffusion media. Commercial gas diffusion material has been shown to have lower porosity than

electrospun fibers and poorer mass transport properties than both SGL and electrospun materials.

5 Conclusion

5.1 Summary of results

Zinc – air batteries offer many advantages over existing forms of large-scale energy storage. The inherent safety of their electrochemistry along with affordable anode and cathode materials make them particularly attractive. Improving the energy and power density of zinc – air batteries and reducing the cost of catalysts in the cathode are critical for the technology to be adopted at scale. The work in this thesis focused on developing and characterizing new cathode architectures that improve battery performance by optimizing oxygen transport in the gas diffusion layer and electrolyte invasion in the catalyst layer.

Hydrophobic nanoscale carbon fibers were produced by electrospinning. These sheets of fiber were then carbonized, coated with PTFE, and used as the gas diffusion layer in novel air electrodes produced using electrospinning and electrospraying techniques. Mats of these fibers were shown to have a high porosity and offer a 55% improvement in oxygen diffusion over the conventional powder/binder materials currently being used as gas diffusion layers. PTFE loading of 10wt% was shown to increase the breakthrough pressure of the electrospun mat to 146 kPa and applying a microporous layer of carbon with 50wt% PTFE further increased breakthrough pressure to 192 kPa. Catalyst layers containing 40wt% Pt on carbon powder were electrosprayed onto the MPL; PTFE and Nafion were both used as binder materials with loadings of 25wt% and 30wt% respectively. Catalyst loading of .4mg/cm^2 was targeted for all materials produced in this work, as it is the current

industry standard. Catalyst layers were electrosprayed onto commercially available GDLs and onto a carbon powder / PTFE backing layer to compare performance.

Electrochemical testing revealed that more development of electrospun and electrosprayed GDEs is required for them to be viable for zinc air battery applications. Though the individual components of the electrospun/electrosprayed material showed improved mass transfer characteristics, polarization curve experiments showed that they underperformed commercial electrode materials. However, an SGL 24 BC gas diffusion layer with electrosprayed catalyst outperformed the commercial electrode substantially, indicating the potential of electrosprayed catalyst layers in zinc air cells. This result also suggests that the electrospun and electrosprayed material may be hindered by PTFE in the microporous layer or interfaces between the GDE's components, and not the catalyst layer.

An electrospun and electrosprayed cathode with bare carbon fibers serving as a gas diffusion layer was developed to investigate the impact of PTFE loading on the internal resistance of the cell. Polarization curve experiments with this electrode showed that it out-performed the commercial material. This result is encouraging, suggesting that electrospun/electrosprayed cathode materials offer mass transfer and electrochemical performance improvements over the commercially available materials, but better current collector integration and/or PTFE alternatives need to be developed to fully take advantage of them. Polarization curves with limited oxygen concentration further demonstrated that electrospun/electrosprayed electrodes offer better mass transport than the reference cathodes that use a powder/binder gas diffusion layer.

5.2 Recommended work

Though this research has demonstrated the promise of electrosprayed catalyst layers in zinc air batteries and the favorable properties of electrospun materials, more research is required to fully explore their potential in zinc air battery applications. The electrochemical performance of the electrospun electrodes with PTFE coated fibers is not reflective of their high diffusivity, and electrosprayed catalyst layers were shown to perform well when applied to SGL gas diffusion layers. To answer why the electrospun materials performed poorly, X-ray tomography might be used to image the interface between spun fibers and MPL, and the MPL/CL interface. SEM images with energy dispersive x-ray (EDX) may be used to better understand the distribution of PTFE on the fibers, highlighting portions of the image where fluorine is present.

Electrochemical characterization of the promising cathode materials developed in this work is recommended so that ohmic losses due to internal cell resistance are minimized. Electrochemical impedance spectroscopy experiments to determine characteristics such as the solution-solid interface resistance and charge transfer resistance for each electrode would be useful in understanding electrode performance and refining electrode design. As cathode design progresses longevity and cycle testing will be important to understand the durability and degradation mechanisms for novel cathode materials.

Conductivity of the fibers and integration of the current collector with the gas diffusion layer is critical to reduce ohmic losses in the cell. These aspects of electrode design were not addressed in this work, though they must be for electrospun and electrosprayed materials to be utilized at scale. Optimizing the carbonization process

is a means to improve fiber conductivity and developing a method to increase fiber contact with the current collector would help reduce ohmic losses as well. Alternative methods to alter the surface energy of the electrospun fibers may be used to develop hydrophobic electrospun GDLs without requiring PTFE loading.

The catalyst, catalyst loading, and catalyst layer compositions studied in this work were all based on current standards. Electrospraying has been shown to be a viable catalyst layer application method for zinc air cells, and more work can be done optimizing the composition of the electrosprayed catalyst layer. Investigating electrospraying novel, non-platinum group metals may be a path to developing cost effective zinc air cathodes with improved electrochemical surface area. Alternative surface treatments to create hydrophobic electrospun gas diffusion layers may be a path to improving the conductivity of electrospun electrodes and should be explored.

6 References

[1] "Global energy and CO2 emissions in 2020 – Global Energy Review 2020 – Analysis - IEA." https://www.iea.org/reports/global-energy-review-2020/global-energy-and-co2-emissions-in-2020 (accessed Nov. 04, 2020).

[2] M. D. Leonard, E. E. Michaelides, and D. N. Michaelides, "Energy storage needs for the substitution of fossil fuel power plants with renewables," *Renew. Energy*, vol. 145, pp. 951–962, 2020, doi: 10.1016/j.renene.2019.06.066.

[3] APS, "Challenges of Electricity Storage Technologies: A Report from the APS Panel on Public Affairs Committee on Energy and Environment," no. May, p. 23, 2007.

[4] J. Zhang, Q. Zhou, Y. Tang, L. Zhang, and Y. Li, "Zinc-air batteries: Are they ready for prime time?," *Chem. Sci.*, vol. 10, no. 39, pp. 8924–8929, 2019, doi: 10.1039/c9sc04221k.

[5] S. L. B. T.-N. and F. D. in C. Suib, Ed., "New and Future Developments in Catalysis," Amsterdam: Elsevier, 2013, p. iii.

[6] Z. Zhao, X. Fan, J. Ding, W. Hu, C. Zhong, and J. Lu, "Challenges in Zinc Electrodes for Alkaline Zinc-Air Batteries: Obstacles to Commercialization," *ACS Energy Lett.*, vol. 4, no. 9, pp. 2259–2270, 2019, doi: 10.1021/acsenergylett.9b01541.

[7] D. Stock, S. Dongmo, J. Janek, and D. Schröder, "Benchmarking Anode Concepts: The Future of Electrically Rechargeable Zinc-Air Batteries," *ACS Energy Lett.*, vol. 4, no. 6, pp. 1287–1300, 2019, doi: 10.1021/acsenergylett.9b00510.

[8] A. R. Mainar *et al.*, "An overview of progress in electrolytes for secondary zinc-air batteries and other storage systems based on zinc," *J. Energy Storage*, vol. 15,

pp. 304–328, 2018, doi: 10.1016/j.est.2017.12.004.

[9] S. Müller, F. Holzer, and O. Haas, “Optimized zinc electrode for the rechargeable zinc-air battery,” *J. Appl. Electrochem.*, vol. 28, no. 9, pp. 895–898, 1998, doi: 10.1023/A:1003464011815.

[10] V. Caramia and B. Bozzini, “Materials science aspects of zinc-air batteries: A review,” *Mater. Renew. Sustain. Energy*, vol. 3, no. 2, 2014, doi: 10.1007/s40243-014-0028-3.

[11] A. R. Mainar, L. C. Colmenares, H. J. Grande, and J. A. Blázquez, “Enhancing the cycle life of a Zinc–air battery by means of electrolyte additives and zinc surface protection,” *Batteries*, vol. 4, no. 3, 2018, doi: 10.3390/batteries4030046.

[12] B. Amunátegui, A. Ibáñez, M. Sierra, and M. Pérez, “Electrochemical energy storage for renewable energy integration: zinc-air flow batteries,” *J. Appl. Electrochem.*, vol. 48, no. 6, pp. 627–637, 2018, doi: 10.1007/s10800-017-1133-7.

[13] V. Neburchilov *et al.*, “A review on air cathodes for zinc-air fuel cells,” *Mater. Renew. Sustain. Energy*, vol. 8, no. 2, pp. 9–13, 2010, doi: 10.1007/s40243-014-0028-3.

[14] O. Kwon *et al.*, “Transparent Bendable Secondary Zinc-Air Batteries by Controlled Void Ionic Separators,” *Sci. Rep.*, vol. 9, no. 1, pp. 1–9, 2019, doi: 10.1038/s41598-019-38552-4.

[15] G. M. Tomboc, P. Yu, T. Kwon, K. Lee, and J. Li, “Ideal design of air electrode-A step closer toward robust rechargeable Zn-air battery,” *APL Mater.*, vol. 8, no. 5, 2020, doi: 10.1063/5.0005137.

[16] Y. Wen *et al.*, “Electrospinning as a route to advanced carbon fibre materials for selected low-temperature electrochemical devices : a review,” *J. Energy Chem.*, 2020, doi: 10.1016/j.jechem.2020.11.014.

[17] A. M. Chaparro, M. A. Folgado, P. Ferreira-Aparicio, A. J. Martín, I. Alonso-Álvarez, and L. Daza, “Properties of Catalyst Layers for PEMFC Electrodes Prepared by Electrospray Deposition,” *J. Electrochem. Soc.*, vol. 157, no. 7, p. B993, 2010, doi: 10.1149/1.3425740.

[18] S. Liu, M. Kok, Y. Kim, J. L. Barton, F. R. Brushett, and J. Gostick, “Evaluation of Electrospun Fibrous Mats Targeted for Use as Flow Battery Electrodes,” *J. Electrochem. Soc.*, vol. 164, no. 9, pp. A2038–A2048, 2017, doi: 10.1149/2.1301709jes.

[19] B. Zhang, F. Kang, J. M. Tarascon, and J. K. Kim, “Recent advances in electrospun carbon nanofibers and their application in electrochemical energy storage,” *Prog. Mater. Sci.*, vol. 76, pp. 319–380, 2016, doi: 10.1016/j.pmatsci.2015.08.002.

[20] N. R. Canada, “Energy Fact Book.” p. 122, 2020.

[21] F. Cheng, S. Willard, J. Hawkins, B. Arellano, O. Lavrova, and A. Mammoli, “Applying battery energy storage to enhance the benefits of photovoltaics,” *2012 IEEE Energytech, Energytech 2012*, pp. 1–5, 2012, doi: 10.1109/EnergyTech.2012.6304684.

[22] S. Ambec and C. Crampes, “Electricity provision with intermittent sources of energy,” *Resour. Energy Econ.*, vol. 34, no. 3, pp. 319–336, 2012, doi: 10.1016/j.reseneeco.2012.01.001.

[23] M. Aneke and M. Wang, “Energy storage technologies and real life applications – A state of the art review,” *Appl. Energy*, vol. 179, pp. 350–377, 2016, doi: 10.1016/j.apenergy.2016.06.097.

[24] M. A. Rahman, X. Wang, and C. Wen, “High Energy Density Metal-Air Batteries: A Review,” *J. Electrochem. Soc.*, vol. 160, no. 10, pp. A1759–A1771, 2013, doi: 10.1149/2.062310jes.

[25] B. Liu *et al.*, “Effect of polytetrafluoroethylene (PTFE) in current collecting layer on the performance of zinc-air battery,” *Prog. Nat. Sci. Mater. Int.*, no. September, pp. 1–7, 2020, doi: 10.1016/j.pnsc.2020.09.012.

[26] Z. Ma *et al.*, “Degradation characteristics of air cathode in zinc air fuel cells,” *J. Power Sources*, vol. 274, pp. 56–64, 2015, doi: 10.1016/j.jpowsour.2014.10.030.

[27] J. Yu, B. Q. Li, C. X. Zhao, J. N. Liu, and Q. Zhang, “Asymmetric Air Cathode Design for Enhanced Interfacial Electrocatalytic Reactions in High-Performance Zinc–Air Batteries,” *Adv. Mater.*, vol. 32, no. 12, pp. 1–7, 2020, doi: 10.1002/adma.201908488.

[28] K. Xu, A. Loh, B. Wang, and X. Li, “Enhancement of Oxygen Transfer by Design Nickel Foam Electrode for Zinc−Air Battery,” *J. Electrochem. Soc.*, vol. 165, no. 5, pp. A809–A818, 2018, doi: 10.1149/2.0361805jes.

[29] P. Wang, L. Wan, Y. Lin, and B. Wang, “Construction of mass-transfer channel in air electrode with bifunctional catalyst for rechargeable zinc-air battery,” *Electrochim. Acta*, vol. 320, p. 134564, 2019, doi: 10.1016/j.electacta.2019.134564.

[30] S. Megelski, J. S. Stephens, D. Bruce Chase, and J. F. Rabolt, “Micro- and

nanostructured surface morphology on electrospun polymer fibers," *Macromolecules*, vol. 35, no. 22, pp. 8456–8466, 2002, doi: 10.1021/ma020444a.

[31] Y. M. Shin, M. M. Hohman, M. P. Brenner, and G. C. Rutledge, "Experimental characterization of electrospinning: The electrically forced jet and instabilities," *Polymer (Guildf).*, vol. 42, no. 25, pp. 09955–09967, 2001, doi: 10.1016/s0032-3861(01)00540-7.

[32] K. B. Wiles, V. A. Bhanu, A. J. Pasquale, T. E. Long, and J. E. McGrath, "Determination of reactivity ratios for acrylonitrile/methyl acrylate radical copolymerization via non-linear methodologies using real time FTIR.," *Polym. Prepr. (American Chem. Soc. Div. Polym. Chem.*, vol. 42, no. 2, pp. 608–609, 2001, [Online]. Available: https://vtechworks.lib.vt.edu/handle/10919/34888.

[33] S. Arbab, A. Teimoury, H. Mirbaha, D. C. Adolphe, B. Noroozi, and P. Nourpanah, "Optimum stabilization processing parameters for polyacrylonitrile-based carbon nanofibers and their difference with carbon (micro) fibers," *Polym. Degrad. Stab.*, vol. 142, pp. 198–208, 2017, doi: 10.1016/j.polymdegradstab.2017.06.026.

[34] M. S. A. Rahaman, A. F. Ismail, and A. Mustafa, "A review of heat treatment on polyacrylonitrile fiber," *Polym. Degrad. Stab.*, vol. 92, no. 8, pp. 1421–1432, 2007, doi: 10.1016/j.polymdegradstab.2007.03.023.

[35] J. Shim *et al.*, "Preparation and characterization of electrospun LaCoO3 fibers for oxygen reduction and evolution in rechargeable Zn–air batteries," *J. Appl. Electrochem.*, vol. 45, no. 9, pp. 1005–1012, Sep. 2015, doi: 10.1007/s10800-

015-0868-2.

[36] G. S. Park, J. S. Lee, S. T. Kim, S. Park, and J. Cho, “Porous nitrogen doped carbon fiber with churros morphology derived from electrospun bicomponent polymer as highly efficient electrocatalyst for Zn-air batteries,” *J. Power Sources*, vol. 243, pp. 267–273, 2013, doi: 10.1016/j.jpowsour.2013.06.025.

[37] C. L. Huang, P. Y. Wang, and Y. Y. Li, “Fabrication of electrospun CO2 adsorption membrane for zinc-air battery application,” *Chem. Eng. J.*, vol. 395, no. April, p. 125031, 2020, doi: 10.1016/j.cej.2020.125031.

[38] G. Zainab *et al.*, “Free-standing, spider-web-like polyamide/carbon nanotube composite nanofibrous membrane impregnated with polyethyleneimine for CO2 capture,” *Compos. Commun.*, vol. 6, no. May, pp. 41–47, 2017, doi: 10.1016/j.coco.2017.09.001.

[39] I. Ahmad *et al.*, “Robust fused aromatic pyrazine-based two-dimensional network for stably cocooning iron nanoparticles as an oxygen reduction electrocatalyst,” *Nano Energy*, vol. 56, pp. 581–587, 2019, doi: 10.1016/j.nanoen.2018.12.007.

[40] S. Martin, P. L. Garcia-Ybarra, and J. L. Castillo, “Electrospray deposition of catalyst layers with ultra-low Pt loadings for PEM fuel cells cathodes,” *J. Power Sources*, vol. 195, no. 9, pp. 2443–2449, 2010, doi: 10.1016/j.jpowsour.2009.11.092.

[41] X. Y. Yuan, Y. Y. Zhang, C. Dong, and J. Sheng, “Morphology of ultrafine polysulfone fibers prepared by electrospinning,” *Polym. Int.*, vol. 53, no. 11, pp. 1704–1710, 2004, doi: 10.1002/pi.1538.

[42] C. S. Ki, D. H. Baek, K. D. Gang, K. H. Lee, I. C. Um, and Y. H. Park, "Characterization of gelatin nanofiber prepared from gelatin-formic acid solution," *Polymer (Guildf).*, vol. 46, no. 14, pp. 5094–5102, 2005, doi: 10.1016/j.polymer.2005.04.040.

[43] A. L. Andrady, *Science and technology of polymer nanofibers*. John Wiley & Sons, 2008.

[44] S. Y. Gu and J. Ren, "Process optimization and empirical modeling for electrospun poly(D,L-lactide) fibers using response surface methodology," *Macromol. Mater. Eng.*, vol. 290, no. 11, pp. 1097–1105, 2005, doi: 10.1002/mame.200500215.

[45] S. V. Fridrikh, J. H. Yu, M. P. Brenner, and G. C. Rutledge, "Controlling the Fiber Diameter during Electrospinning," *Phys. Rev. Lett.*, vol. 90, no. 14, p. 4, 2003, doi: 10.1103/PhysRevLett.90.144502.

[46] L. Huang, N. N. Bui, S. S. Manickam, and J. R. McCutcheon, "Controlling electrospun nanofiber morphology and mechanical properties using humidity," *J. Polym. Sci. Part B Polym. Phys.*, vol. 49, no. 24, pp. 1734–1744, 2011, doi: 10.1002/polb.22371.

[47] E. Zussman *et al.*, "Mechanical and structural characterization of electrospun PAN-derived carbon nanofibers," *Carbon N. Y.*, vol. 43, no. 10, pp. 2175–2185, 2005, doi: 10.1016/j.carbon.2005.03.031.

[48] S. Brunauer, P. H. Emmett, and E. Teller, "Adsorption of Gases in Multimolecular Layers," *J. Am. Chem. Soc.*, vol. 60, no. 2, pp. 309–319, 1938, doi: 10.1021/ja01269a023.

[49] J. Rouquerol, P. Llewellyn, and F. Rouquerol, “Is the BET equation applicable to microporous adsorbents?,” *Stud. Surf. Sci. Catal.*, vol. 160, no. December, pp. 49–56, 2007, doi: 10.1016/s0167-2991(07)80008-5.

[50] J. T. Gostick, M. A. Ioannidis, M. W. Fowler, and M. D. Pritzker, “Wettability and capillary behavior of fibrous gas diffusion media for polymer electrolyte membrane fuel cells,” *J. Power Sources*, vol. 194, no. 1, pp. 433–444, 2009, doi: 10.1016/j.jpowsour.2009.04.052.

[51] Y. Kim and J. T. Gostick, “Measuring effective diffusivity in porous media with a gasket-free, radial arrangement,” *Int. J. Heat Mass Transf.*, vol. 129, pp. 1023–1030, 2019, doi: 10.1016/j.ijheatmasstransfer.2018.10.054.

[52] D. Kramer *et al.*, “Electrochemical diffusimetry of fuel cell gas diffusion layers,” *J. Electroanal. Chem.*, vol. 612, no. 1, pp. 63–77, 2008, doi: 10.1016/j.jelechem.2007.09.014.

[53] R. Flückiger, S. A. Freunberger, D. Kramer, A. Wokaun, G. G. Scherer, and F. N. Büchi, “Anisotropic, effective diffusivity of porous gas diffusion layer materials for PEFC,” *Electrochim. Acta*, vol. 54, no. 2, pp. 551–559, 2008, doi: 10.1016/j.electacta.2008.07.034.

[54] J. Crank, *The mathematics of diffusion*. Oxford university press, 1979.

[55] L. Shen and Z. Chen, “Critical review of the impact of tortuosity on diffusion,” *Chem. Eng. Sci.*, vol. 62, no. 14, pp. 3748–3755, 2007, doi: 10.1016/j.ces.2007.03.041.

[56] D. R. P. Morris and J. T. Gostick, “Determination of the in-plane components of the electrical conductivity tensor in PEM fuel cell gas diffusion layers,”

Electrochim. Acta, vol. 85, pp. 665–673, 2012, doi: 10.1016/j.electacta.2012.08.083.

[57] L. J. Van der Pauw, "VDP_PRR_13_1.pdf," *Philips Research Reports*, vol. 13. pp. 1–9, 1958.

[58] M. Andisheh-Tadbir, M. El Hannach, E. Kjeang, and M. Bahrami, "An analytical relationship for calculating the effective diffusivity of micro-porous layers," *Int. J. Hydrogen Energy*, vol. 40, no. 32, pp. 10242–10250, 2015, doi: 10.1016/j.ijhydene.2015.06.067.

[59] M. N. Islam, U. Shrivastava, M. Atwa, X. Li, V. Birss, and K. Karan, "Highly Ordered Nanoporous Carbon Sca ff old with Controllable Wettability as the Microporous Layer for Fuel Cells," no. i, 2020, doi: 10.1021/acsami.0c10755.

7 Appendix

7.1 Supplemental Figures

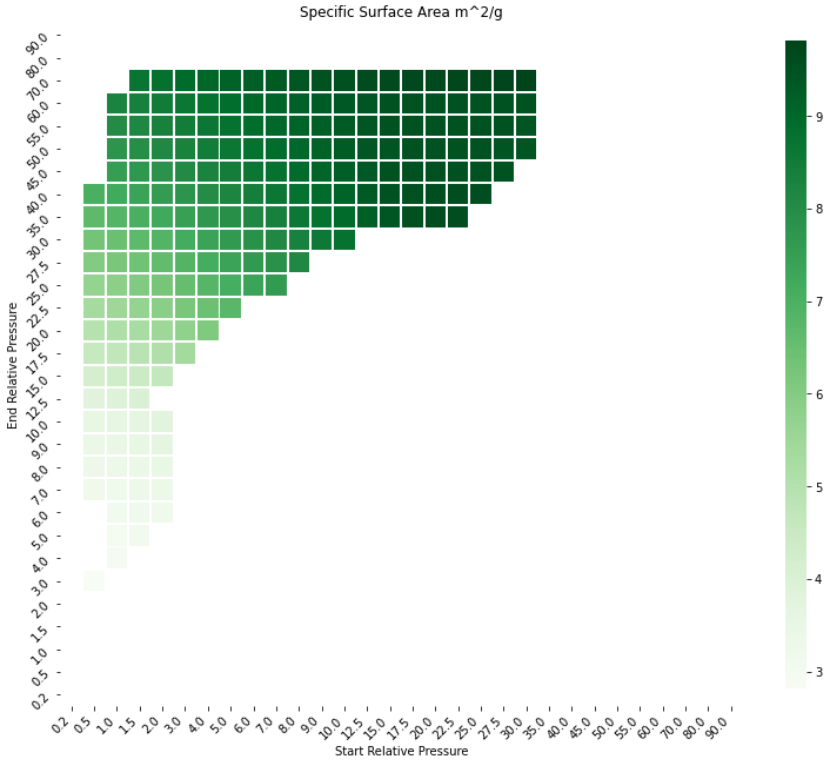

Figure 34 Valid specific surface area values for PTFE coated electrospun carbon fibers

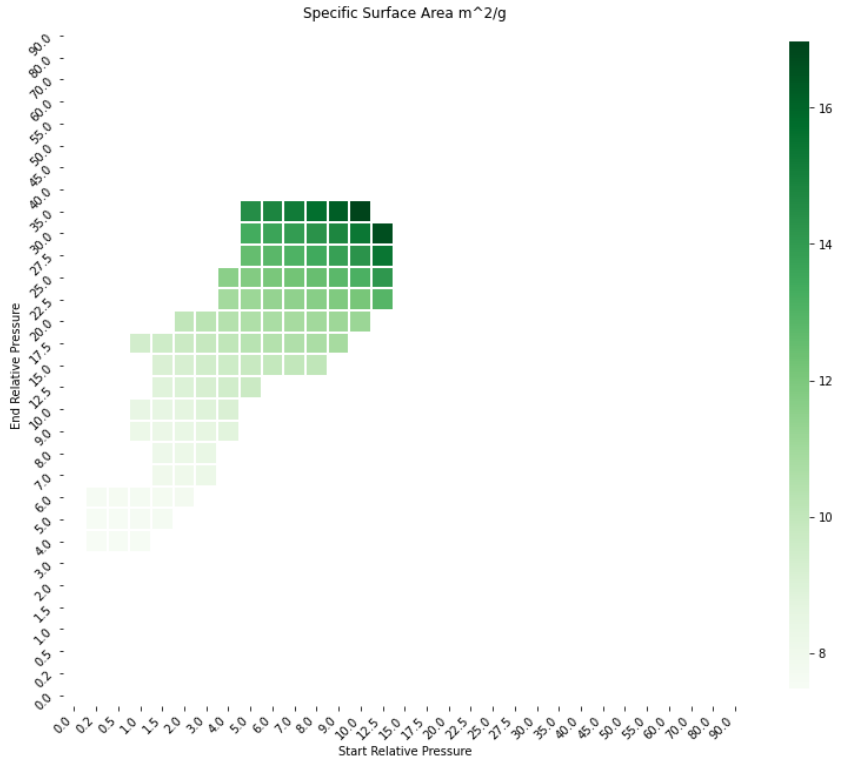

Figure 35 Valid specific surface area values for PTFE coated electrospun carbon fibers with an electrosprayed MPL

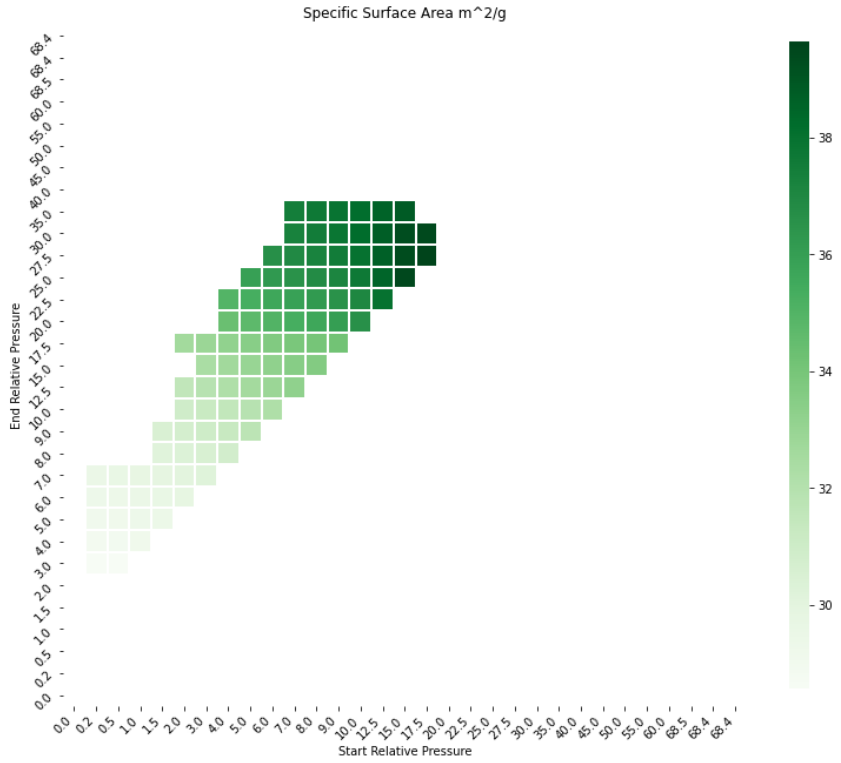

Figure 36 Valid specific surface area values for PTFE coated electrospun carbon fibers with an electrosprayed MPL and CL